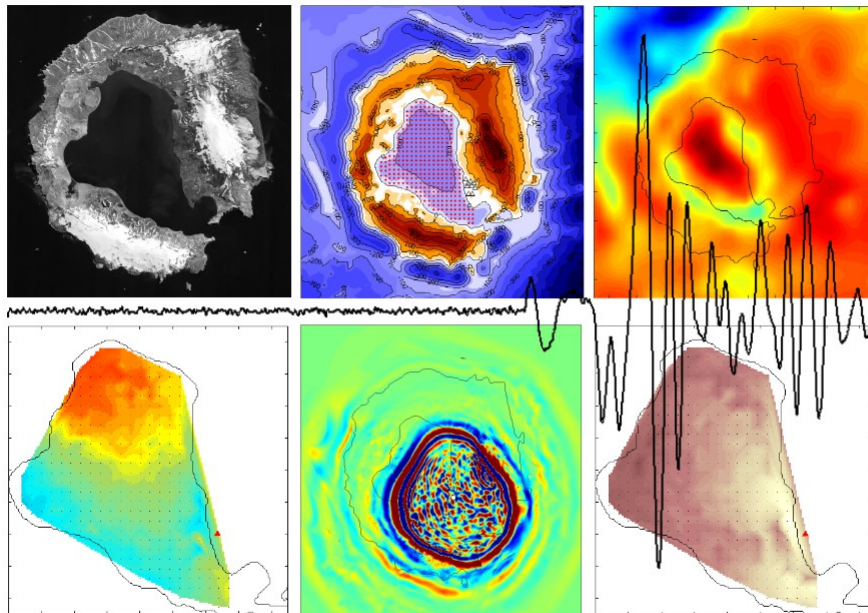# UNIVERSIDAD DE GRANADA

Máster En Geofísica y Meteorología

Curso 2015-2016

Trabajo de Fin de Máster

STUDY OF WAVE PROPAGATION ANOMALIES AT DECEPTION ISLAND VOLCANO BY USING NUMERICAL SIMULATIONS AND ARRAY TECHNIQUES

Itahisa Nesoya González Álvarez

UNIVERSIDAD DE GRANADA

INSTITUTO ANDALUZ DE GEOFÍSICA

Máster En Geofísica y Meteorología

Curso 2015-2016

GEOMET

_____

Autora

Itahisa Nesoya González Álvarez

Trabajo de Fin de Máster dirigido por

el Dr. Javier Almendros González

Acknowledgments

Index

1. Introduction.

The propagation of seismic waves in volcanic environments is usually affected by their typical sharp topographies as well as by multiple kinds of heterogeneities that cause them to attenuate, deviate from their initial path and/or change their velocity (and, consequently, to alter their traveltime), either by being reflected, refracted or diffracted. The study of such waves allows to obtain valuable information about the inner structure of the volcano and its dynamics (e.g. Kumagai and Chouet, 1999; Chouet *et al.*, 2003; Di Grazia *et al.*, 2009; Patanè *et al.*, 2006; 2013). For example, traveltime tomography uses the delays induced on P and S waves by those heterogeneities to characterize the velocity structure of the area (e.g. Benz *et al.* 1996; Dawson *et al.* 1999; Patanè *et al.* 2002; Monteiller *et al.* 2005; Vanorio *et al.* 2005; Park *et al.* 2007; Koulakov *et al.* 2009; Zandomeneghi *et al.* 2009).

Seismic arrays, or seismic antennas, are defined as a group of similar and syncronized seismic stations arranged in a geometric pattern over a homogeneous area. By comparing the seismograms registered at each individual station, seismic arrays allow to estimate temporal and spatial variations of the propagation properties (usually direction and apparent velocity in the form of the apparent slowness vector) of the waves propagating across the array. Combining several of them can be even more advantageous, as this technique provides also information about the position of the source. As array methods do not require seismic waves to contain clearly differenciated phases, they are an essential tool for volcanic seismicity studies, where seismic signals do not usually show them (e.g., Goldstein & Chouet, 1994; Almendros *et al.*, 1997, 2002; De Luca *et al.*, 1997; Del Pezzo *et al.*, 1997; Saccorotti *et al.*, 1998, 2004).

In 2005, an active-source tomographic experiment was carried out at Deception Island volcano (South Shetland Islands, Antarctica). For that purpose, more than 6000 air gun shots were fired all around the island (including Port Foster, the central bay at its centre), generating seismic waves in the process which were registered by both land and ocean bottom seismometers deployed on and around the island. Those seismic stations were arranged both as individual stations and as part of dense and sparse seismic arrays located along the inner coast of Port Foster. From those high-quality data, Zandomeneghi *et al.* (2009) obtained a high-resolution velocity model of the island and García Yeguas *et al.* (2011) studied the propagation of the seismic waves across the heterogenous medium of the volcano.

Eight of the aforementioned arrays were used by García Yeguas *et al.* (2011) to estimate the apparent slowness vectors of the wavefields generated by the air-gun shots. Since the shot locations were known, they were able to study the wave propagation in detail. Thus, they found important wave propagation anomalies which were hypothesised as being the effect of the velocity structure of the island. These results showed the necessity of taking local velocity structure, topography and bathymetry into account, especially for classical seismology methods, where oversimplified models have been traditionally used, thus ignoring the complexity and heterogeneity of volcanic structures. These authors also pointed out the advantages of modern computational methods, which are capable of effectively including the effects of topography as well as precise velocity structure models in order to perform more accurate simulations of waves propagation.

In the work presented here, I will carry on a series of simulations in order to find out whether the anomalous results obtained by García Yeguas *et al.* in 2011 were caused by the combined effect of the topography and the velocity structure.

2. Geological and tectonic context.

The whole area around Deception Island is tectonically complex. The Bransfield Strait is a 400 km long and 60 km wide NE-SW trending back-arc basin (Figure 1) that developed between the South Shetland Islands and the Antarctic Peninsula due to the subduction of the Phoenix plate beneath the Antarctic plate. About 4 Ma ago, the expansion along the ridge NW of the South Shetland Islands slowed (Christeson *et al.*, 2003) and the subducting slab began rolling back, thus originating an extensional regime in the Bransfield Strait and creating a new microplate, the South Shetland Plate. Today, the expansion rate of the Bransfield Strait is estimated from GPS measurements at around 10 mm/a (Robertson-Maurice *et al.*, 2003; Vuan *et al.*, 2005), which is thought to be also the subduction rate of the mentioned Phoenix plate (Pelayo and Wiens, 1989). Besides this, the transtension along the boundary between the Antarctic and Scotia plates is another source of extension in the area around Deception Island (Galindo-Zaldivar *et al.*, 1996; Klepeis and Lawer, 1996; Lawver *et al.*, 1996; Maestro *et al.*, 2007; Rey *et al.*, 1995; Robertson-Maurice *et al.*, 2003).

Deception Island is a horseshoe-shaped active stratovolcano located in the South Shetland Islands, an archipelago about 120 kilometers northeast of the Antarctic Peninsula, in the Bransfield Strait (Figure 1). It was visited for the first time in 1820 (Newhall & Dzurisin, 1989; González Ferrán, 1995) and there have been over 20 volcanic eruptions ever since (Pallàs *et al.*, 2001; Smellie *et al.* 2002; Bartolini *et al.*,

Figure 1. a) Simplified regional tectonic map of the area around the SSI, showing the major fractures (HFZ for Hero Fracture Zone and SFZ for Shetland Fracture Zone) in the area and type of plate boundaries (from Martí et al., 2013). b) Precise location of Deception Island (from Martí et al., 2013). c) Aerial photo of the island (http://lagc.uca.es/web_lagc/orto.jpg)
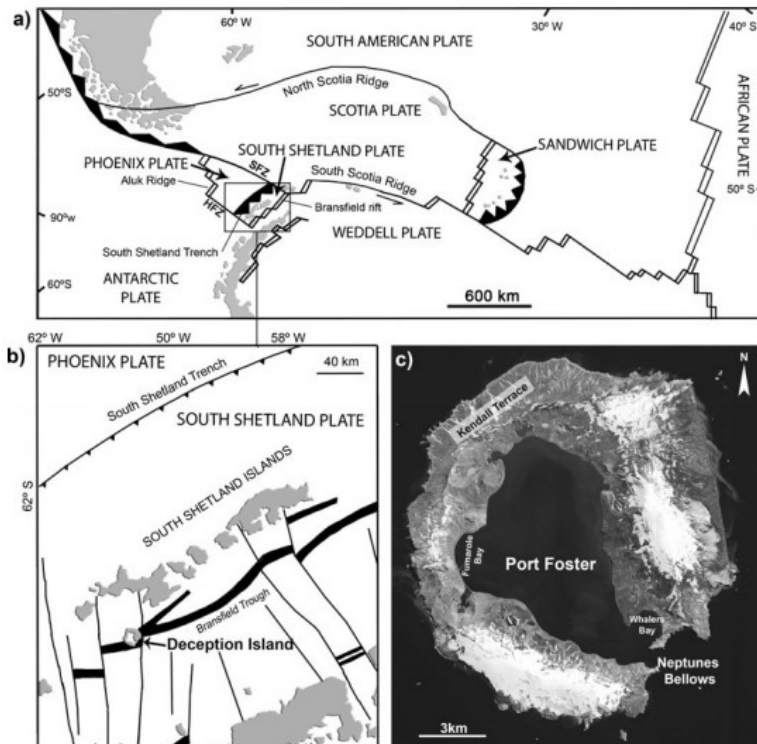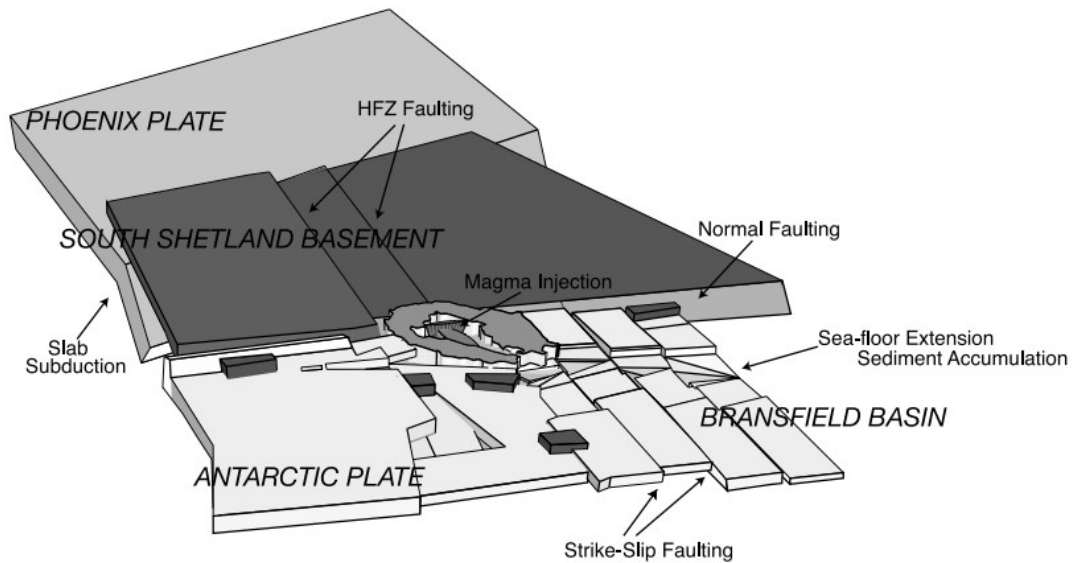
Figure 2. Diagram showing the main structural features of Deception Island region, including the main fault systems in the area (from Zandomeneghi et al., 2009).

2014), making it the most active of volcanoes in the SSI. Most part of Deception Island's surface is covered by glaciers, especially the areas around Mt. Pond (540 m a.s.l.), the highest point of this 13 km wide island, and Mount Kirkwood (450 m a.s.l.). However, its main volcano-tectonic feature is Port Foster, the central, sea-flooded depression with dimensions of about 6x10 km that has been interpreted as a caldera and whose origin has been repeatedly questioned. Based on its apparent circular shape and on the location of the post-caldera vents, some authors suggest that a major eruption took place and caused the collapse around a ring fault (Hawkes, 1961; González-Ferrán and Katsui, 1970; Baker *et al.*, 1975; Walker, 1984; Smellie, 1988, 1989) or a series of intersecting faults (Smellie 2001; Smellie *et al.* 2002). Other authors, however, consider that the distribution of the local seismicity along the main structural trends and fault sets suggests that the origin of Port Foster is not related to any volcanic event, being it formed instead by the progressive extension along the sets of normal faults that control the local tectonics (Martí *et al.*, 1996; Smellie *et al.*, 2002; Lopes *et al.*, 2015).

Two major fault systems, trending NE-SW and NNW-SSE respectively (approximately perpendicular to each other), are present in the island and have an important effect on the local tectonics (Paredes *et al.*, 2006). The former is consistent with the expansion axis of the Bransfield Strait and some of the most recent eruptive centres appear to be aligned with this direction (De Rosa *et al.*, 1995). However, the shape of Costa Recta, on the eastern side of the island, seems to be controlled by the second fault set (Fernández-Ibáñez *et al.*, 2005; Maestro *et al.*, 2007). Deformation studies in the island have shown contemporaneous activity at both systems and, on occasion, a slow uplifting of the floor of the northern sector of Port Foster which has been attributed both to rapid accumulation of sediments and to the expansion of the magma chamber located below the caldera (Dietrich *et al.*, 2001; Robertson Maurice *et al.*, 2003; Cooper *et al.*, 1999).

2.1. Volcanic activity.

Analysis of the exposed rocks at Deception Island show that they have normal magnetic polarity, thus indicating they are not older than 0.75 Ma (Baker *et al.*, 1975; Valencio *et al.*, 1979; Keller *et al.*, 2002). However, based on tephrochronological studies, Smellie (2001) suggested a more recent origin for the subaerial part of the island.

The last six eruptive episodes took place from 1840 to 1971, with their centres (multiple, on occasions) generally located near the coast around Port Foster either in shallow water or onshore (Simkin and Siebert, 2002; Baker *et al.*, 1969, 1975; Smellie, 1988, 2002), being the one happening in 1969 the only one to take place beneath glacier ice (Baker *et al.*, 1975). The observed eruptive styles at Deception Island range from magmatic strombolian explosions (1842, 1969) to phreatomagmatic/surtseyan eruptions (1967, 1970) (De Rosa *et al.*, 1995; Smellie *et al.*, 2002). Currently, evidences of volcanic activity in the island include fumaroles, hot soils due to the presence of high temperature groundwater, and seismicity (e.g. Ortiz *et al.*1992, 1997; Rey *et al.* 1995; Cooper *et al.*1998; Ibáñez *et al.*2000, 2003a, b; Smellie, 1990; Ortiz *et al.*, 1992).

Recent studies have shown that the fault systems present in the island may have a major role in its volcanic activity (Zandhomenegi *et al.*, 2009). The extensional regime around the island make it easier for the magma to rise from the mantle. In addition to this, the most recent eruptions have been preceded or happened shortly after earthquakes that were too big to be caused by the eruptive process itself and all those earthquakes seem to have been originated at the major seismogenic zone around Deception Island, which corresponds with the limit between the Bransfield Basin crust and the SSI platform (Robertson-Maurice *et al.*, 2003; Vuan *et al.*, 2005).

2.2. Seismicity.

Since the first Spanish seismic station was installed at Deception Island in 1986, multiple surveys have taken place during the Antarctic summers. Seismic networks and arrays have been deployed, detecting the usual seismic activity around an active volcano, consisting of volcano-tectonic (VT) earthquakes, long period (LP) events, hybrid events or tremor, but also signals corresponding to avalanches, rockfalls or ice cracks (e.g. Alguacil *et al.*, 1999; Almendros *et al.*, 1997;Ibáñez *et al.*, 2000, 2003; Carmona *et al.*, 2012).

-**VT earthquakes** or high-frequency earthquakes are analogous to the tectonic ones: their waveforms are similar and their frequency content range between 2 and 20 Hz, often with clearly distinguishable arrivals of P and S waves, thus enabling the location of their sources by standard methods based on arrival times of seismic phases. VT events occur in swarms (McNutt, 2002) and their origin is related to shear faulting inside the volcanic edifice in response to variations of pressure in the magma reservoir and conduits, rock failure caused by magma intrusions or ascent, or pore pressure effects, hydrofracturing, etc. (McNutt, 2005). They are one of the earliest detectable signs of an upcoming volcanic eruption (e.g. Roman and Cashman, 2006; Patanè *et al.*, 2002), so it is vital to carefully analyse both their spatial and temporal distributions.

-**LP events** or low-frequency earthquakes have frequencies between 0.5 and 5 Hz and are usually linked to fluids and heat dynamics inside the volcano (Chouet, 1996), like magma transport or resonance inside the cracks where it is stored before an eruption or interactions between magma and underground water, even if it has been shown that they can appear also in dry mediums (Bean *et al.*, 2014). These signals are generally emergent and don't show the characteristic P and S phases of VT earthquakes, so they require different analysis techniques. Volcanic eruptions are frequently preceded by or appear in conjunction with this kind of signals, so they are considered precursors to eruptions (Chouet, 1996).

-**Hybrid events** are characterized by two distinct phases: a first high-frequency wave-train (up to 15 Hz and more in some cases) which usually lasts for less than 5 seconds, followed by a low frequency signal (usually less than 10 Hz) almost identical to those observed on LP events that could be interpreted as composed of surface waves (Ibáñez *et al.*, 2000). This kind of events has been observed at several volcanoes around the world (e.g., Ibáñez *et al.*, 2003; Gil Cruz and Chouet, 1997; Neuberg *et al.*, 1998; White *et al.*, 1998; Lahr *et al.*, 1994) and it has been hypothesised that their origin could be the combination of both VT and LP events source mechanisms or the simultaneous occurrence of a VT and a LP events (e.g. Lahr *et al.*, 1994; Ibáñez *et al.*, 2003).

-**Volcanic tremor** is a seismic signal similar to LP events in terms of waveform and freuency content. However, the main attribute of volcanic tremor is its continuity in time, as it can last for months. As in LP, VLP or hybrid signals, it is not possible to distinguish the arrivals of the different body-wave phases and its frequency content is usually restricted to the 0.1-10 Hz band, with one or more sharp peaks on its spectra that have been interpreted as source effects (e.g., Fehler, 1983; Almendros *et al.*, 1997; Hagerty *et al.*, 2000). Tremor has been recorded at many volcanoes all around the world and it has frequently been associated to eruptive dynamics and interplay between fluids and rocks within the volcanic edifice and acknowledged as a common eruption precursor (e.g. Chouet, 1996b; Gresta *et al.*, 1991; Lombardo *et al.*, 1996; Di Grazia *et al.*, 2006; Alparone *et al.*, 2007; Cannata *et al.*, 2008, 2009; Patanè *et al.*, 2008) . The quantitative analysis of these signals in order to obtain information about their origin and characteristics has been a challenge for seismologists, since the loss of coherence between signals from different stations with spacing between them and, therefore, from the source, make classical location methods useless for tremor studies, thus requiring new analysis techniques to obtain information about its origin and characteristics.

At Deception Island, VT earthquakes are usually small (magnitudes below 3) and their temporal distribution is very irregular. In spatial terms, their location appears to be related to the main fracture systems in the island (Vila *et al.*, 1992; Ibáñez *et al.*, 2003a). LP events, however, have been linked to interactions between shallow groundwater reservoirs and the hot rocks surrounding them, usually leading to the resonance of the fluids within the cracks (Almendros *et al.*1997, 1999; Ortiz *et al.*, 1997; Alguacil *et al.*, 1999; Ibáñez *et al.*2000, 2003), but there is also some evidence of microseismic noise being capable of triggering periodic or rhythmic swarms of LPs (Stich *et al.*, 2011 and references therein).
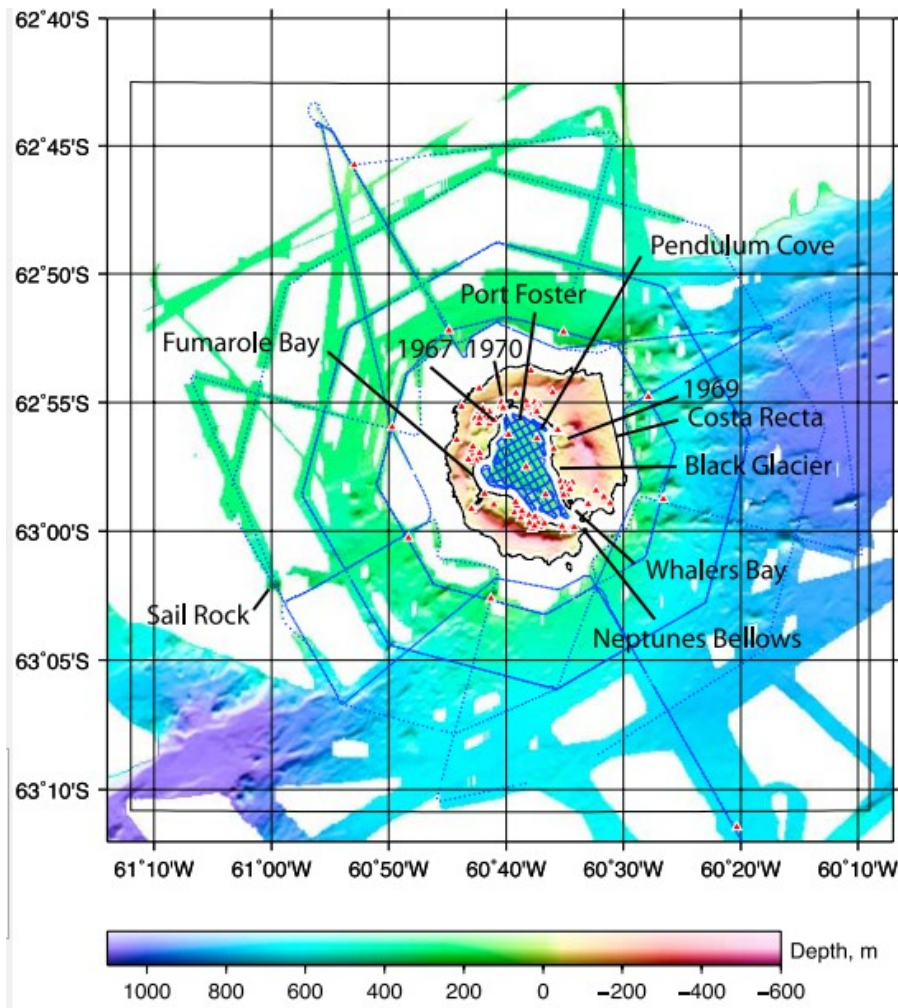
Figure 3. Sketch of the TOMODEC experiment configuration. Red triangles indicate the position of both OBSs and land stations. Blue lines are used to represent shot positions. The location and date of some of the latest eruptions are also marked on the map. (From Zandomeneghi et al., 2009).

3. TOMODEC experiment.

In January 2005, TOMODEC project, an active source tomographic experiment, was carried out at Deception Island volcano. For 2 weeks, nearly 7000 air gun shots were fired from the R/V Hesperides inside Port Foster and around the island and recorded by the seismic network, consisting of both land and ocean bottom seismometers (OBSs) deployed around the island. The main aim of TOMODEC was to obtain a tomographic image of Deception Island and its surroundings, but gravity, magnetic and bathymetry data were also acquired (Barclay *et al.*, 2009; Zandhomenegi *et al.*, 2009). The type of seismicity present in the island (mainly LP events) and the difficulty of establishing and maintaining a permanent seismic network for a long time in such a hostile environment made it necessary to choose an active source tomographic experiment for this purpose instead or carrying on a passive tomographic study.

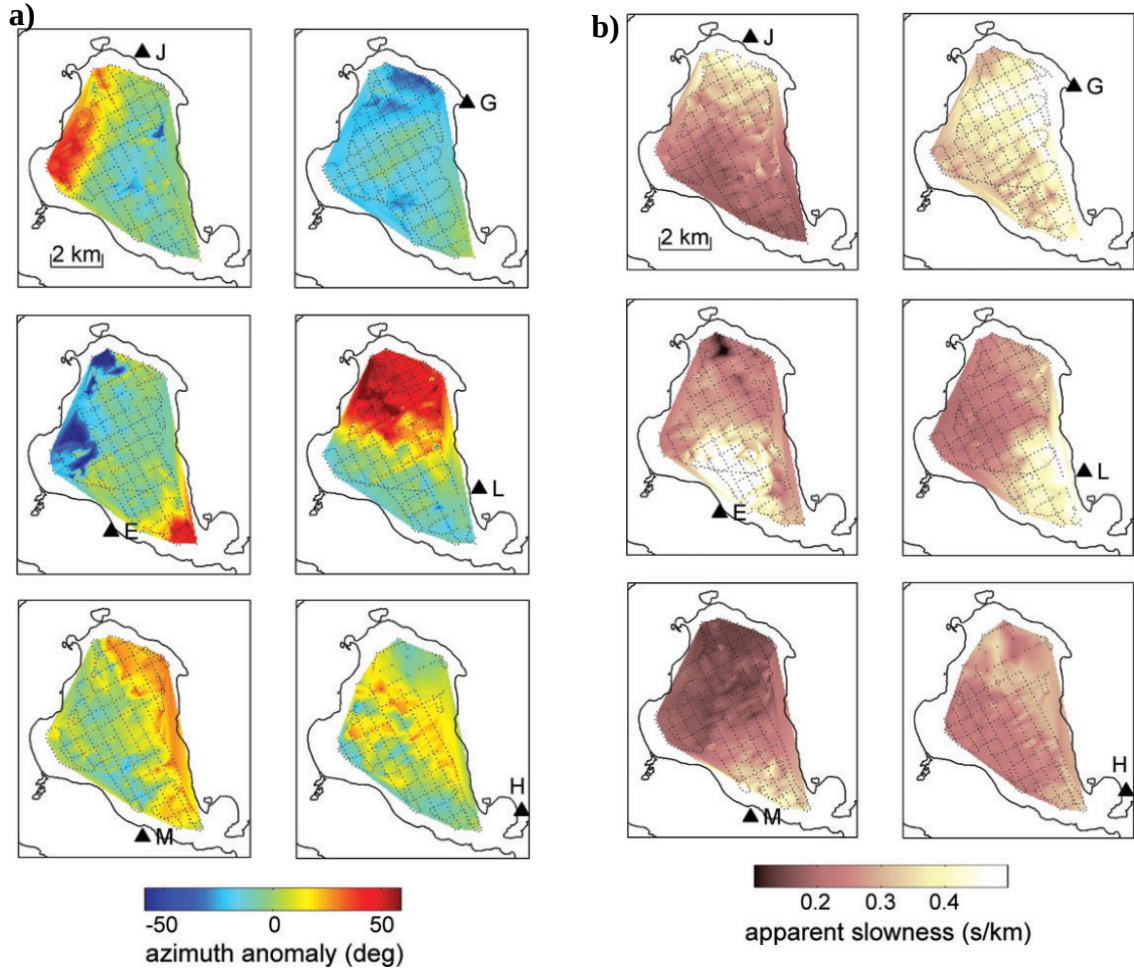*Figure 4. García Yeguas et al. (2011) results for azimuth anomaly (a) and apparent slowness (b) from the air gun shots within Port Foster at six of the eight studied arrays (results for arrays F and K were neglected due to internal inconsistency). In particular, they refer to (1) azimuth anomalies, indicating that the wavefronts propagate in directions different from the shot-array directions; and (2) slowness anomalies, representing waves from sources at similar distances that do not propagate at the same velocity. (From García Yeguas et al., 2011)*

Broadband three component OBSs with added broadband hydrophones were sampled at 125 Hz and disposed in a circular pattern around the island and also inside Port Foster (Zandomeneghi *et al.*, 2009). Their positions were determined by travel time inversion of nearby shots (Creager and Dorman, 1982). 122 lands seismometers were deployed both as dense and sparse seismic arrays (their apertures ranged from 0.2 to 1.3 km) and as autonomous stations (Zandomeneghi *et al.*, 2009; García Yeguas *et al.*, 2011). The arrays had twelve channels connected to short-period seismometers with natural frequency of 4.5 Hz electronically extended to 1 Hz. They were designed and built at the Andalusian Geophysical Institute (Abril, 2007). All data were acquired by sampling at 100 or 125 sps (depending on the type of station) with 24-bit A/D converters (Abril, 2007; Carmona *et al.*, 2012). Within Port Foster, the shots were fired every 120 m along each line of a 500 m grid that covered the whole bay (Zandomeneghi *et al.*, 2009; García Yeguas *et al.*, 2011). Around the island, to avoid gaps in shot coverage, three concentric polygons, two straight lines pointing NNW-SSE and WSW-ENE respectively and radial lines spaced 45º apart were traced, with along-track

distances between shots of 170 m and 340 m (Zandomeneghi *et al.*, 2009; García Yeguas *et al.*, 2011).

The apparent slowness vectors of the first arrivals of the seismic waves generated by the air gun shots during TOMODEC experiment were calculated by García Yeguas *et al.* (2011) by using the Zero Lag Cross Correlation (ZLCC) method, which looks for the maximum array-average cross-correlation values of the aligned waveforms within an apparent slowness grid (see chapter 5 for a more detailed explanation of this method). Seismic arrays methods provide apparent slowness vectors, representing the direction (as the propagation angle measured from north or azimuth) and apparent velocity (or apparent slowness, its inverse) of seismic waves travelling across the array. Their analysis of both azimuth and apparent slowness data at eight different arrays showed anomalies at some of them (Figure 4), in the form of wave fronts propagating in directions different from the shot-array directions in some areas or faster in some directions (thus generating asymmetric wave fronts, instead of radially symmetric ones). In general, positive anomalies appeared in larger and more conspicuous areas than negative ones, being this the most prominent feature. Moreover, it is also remarkable the absence of radial symmetry in the apparent slowness values, shown in the form of shots at similar distances from the array yielding different apparent slowness values. Specifically, figure 4a contains García Yeguas *et al.* (2011) results for azimuth anomaly at each array, defined as the difference between the orientation of the estimated apparent slowness vector and the geometrical azimuth from the shot position to the array centre. Thus, positive values of the azimuth anomaly represent a clockwise rotation of the apparent slowness vector, while small negative anomaly values correspond to counterclockwise rotations. These results, showing several regions where the wavefronts propagate in directions different from the shot-array direction, are interpreted as an illustration of the influence of the medium in wave propagation. Some of them coincide with the hypothesised magma chamber beneath the northern sector of Port Foster, but this feature is not enough to explain all the observed anomalies, which were interpreted as the effect of additional lateral heterogeneities over the ray path. Apparent slowness results for each array are displayed on figure 4b. Considering the position of each array, these results nearly show the expected radial pattern for some arrays. However, significant differences from this model were observed for others, thus indicating again the presence of lateral heterogeneities.

4. Method and data processing.

4.1. The finite-difference method.

Finite difference methods numerically solve differencial equations by approximating the derivatives with finite differences. In this case, the wave propagation equations are solved by using a finely discretized space and small time steps, so that derivatives can be approximated by ratios of differences (e.g. Luo and Schuster, 1990; Virieux, 1984, 1986; Virieux and Madariaga, 1982). The version of the finite-difference method used for this work was developed by Ohmninato and Chouet in 1997, its main
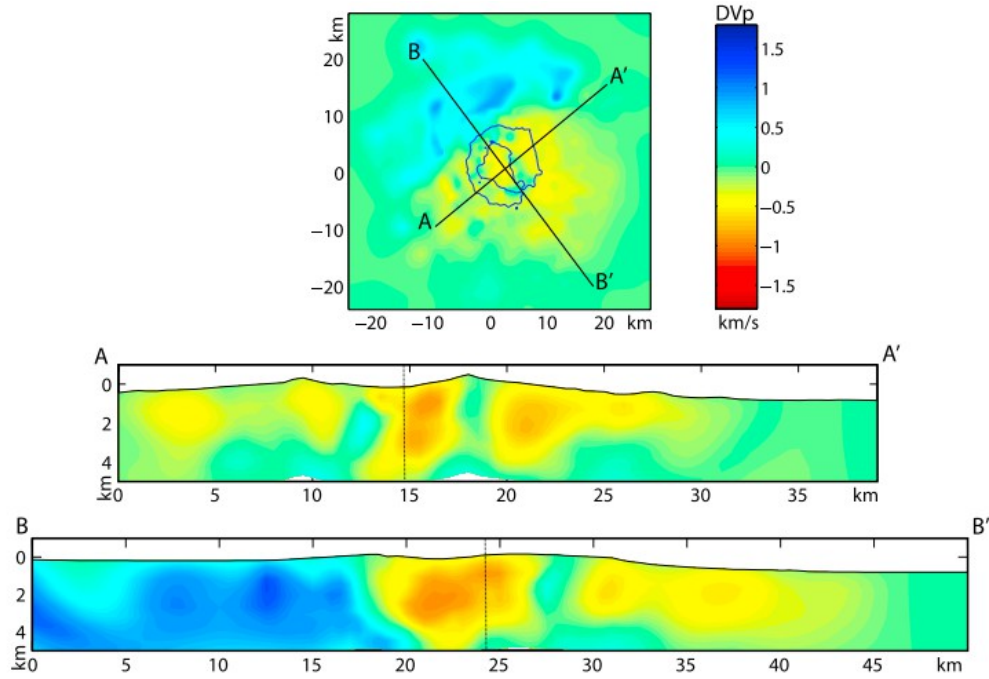
Figure 5. Tomographic velocity perturbations (with respect to the starting model) obtained by Zandomeneghi et al. 0 km depth (top) and vertical slices along the AA' and BB' profiles (middle and bottom) (from Zandomeneghi et al., 2009).

purpose being evaluating the effect of 3D topography on wave propagation in volcanic areas. In the work presented here, I used this method to carry on a series of simulations on a realistic medium which includes Deception Island's topography, bathymetry and 3D velocity structure (obtained by Zandomeneghi *et al.* (2009)).

4.1.1. Computational domain.

The computational domain used for the finite-difference method consisted on a 20 x 20 x 5 km model centred at coordinates (620904, 3017311) UTM, thus containing the entirety of Deception Island. It was divided into 50 x 50 x 50 m cells, thus resulting into a grid with 401 x 401 x 101 nodes. Mt. Pond, the highest point in the island (550 m high, after adjusting its elevation to the nearest node), is also at the top of the domain, then corresponding its bottom to a depth of 4450 m below sea level (Figure 6a, b). To fit to this mesh, topographic, bathymetric and tomographic data had to be interpolated.

Topographic data used to create this model are from the Geographical Service of the Spanish Army (López Martínez et al., 2002), while bathymetric data were obtained from previous models (Barclay et al., 2009) combined with new measurements obtained during TOMODEC experiment. These data needed some modifications in order to acknowledge the presence of water around the island, and so the position of the free surface was changed to a flat surface at sea level for those nodes originally below it (Figure 6b). Appendix 1, at the end of this document, contains the Matlab code written to achieve this purpose and describes the process in more detail.

The velocity structure of the island was obtained by modifying the tomographic data collected by Zandomeneghi *et al.* (2009). In their work, they used the seismic
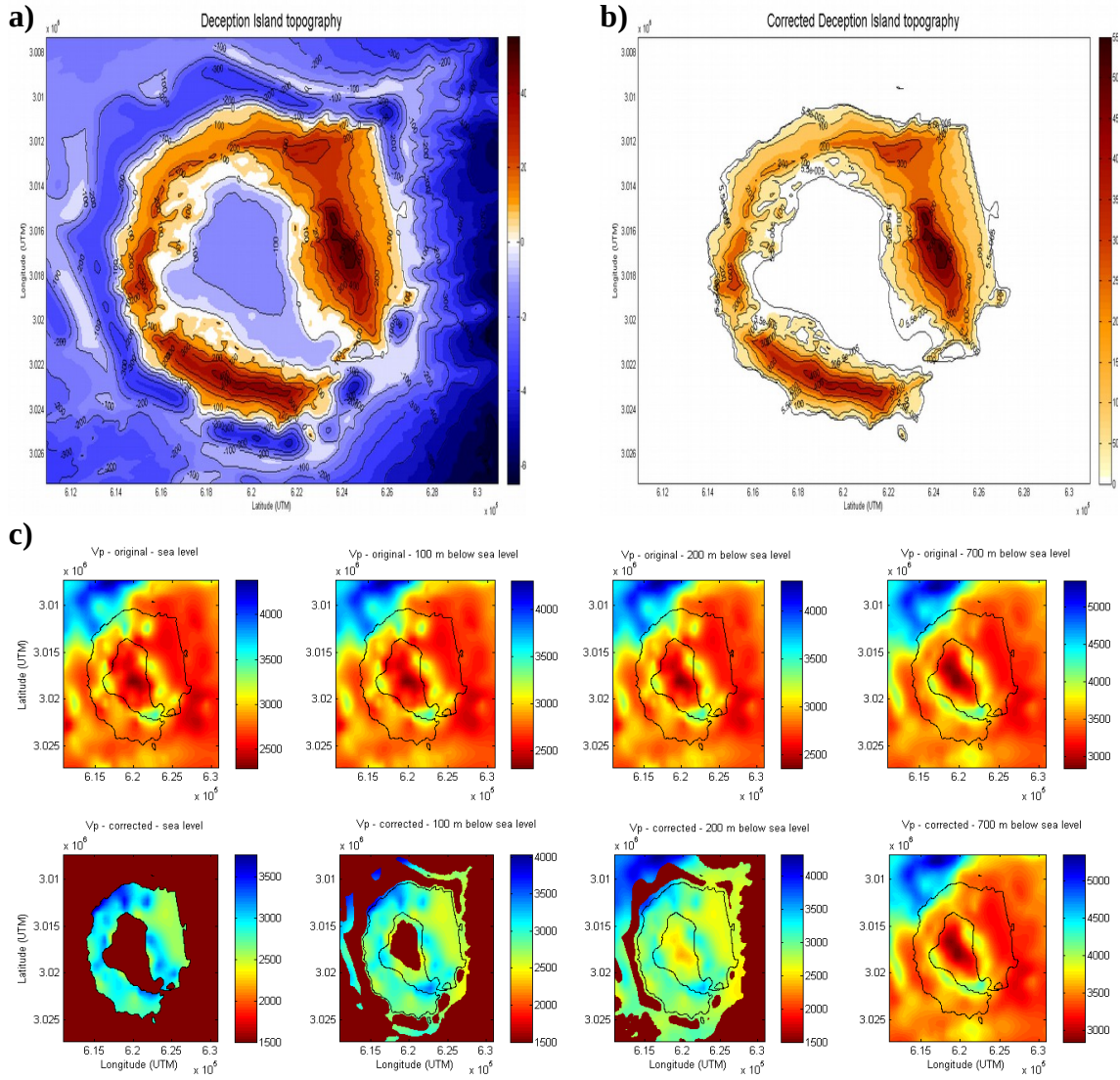
Figure 6. The original topographic model for Deception Island (a) included both topography and bathymetry, but a more realistic model was needed in order to apply the finite-difference method (b). Tomographic data were also modified in order to acknowledge the presence of water around the island. On (c), a series of horizontal sections are showed to illustrate the differences between the original data (upper row) and the corrected ones (bottom row).

tomography code of Toomey *et al.* (1994) for their tomographic inversion, which calculates raypaths and travel times by means of the shortest-path algorithm (Moser, 1991) and uses also LSQR algorithm inversion. They performed two separate inversions, the first one using a sparse grid encompassing all shots and receivers and the second one with a denser grid including only Port Foster. Both results were combined afterwards to produce the overall velocity structure of Deception Island and its surroundings. As a result, they found several low and high velocity anomalies in and around Deception Island (Figure 5), being the most remarkable one a large low-velocity region beneath the northern sector of Port Foster, which was interpreted as the combination of a thick layer (1.2 – 1.4 km thick) of sedimentary deposits and an extensive volume of partial melt that has been related to the presence of a shallow magma chamber that extends from 2 km to at least 5 km depth (Zandomeneghi *et al.*,
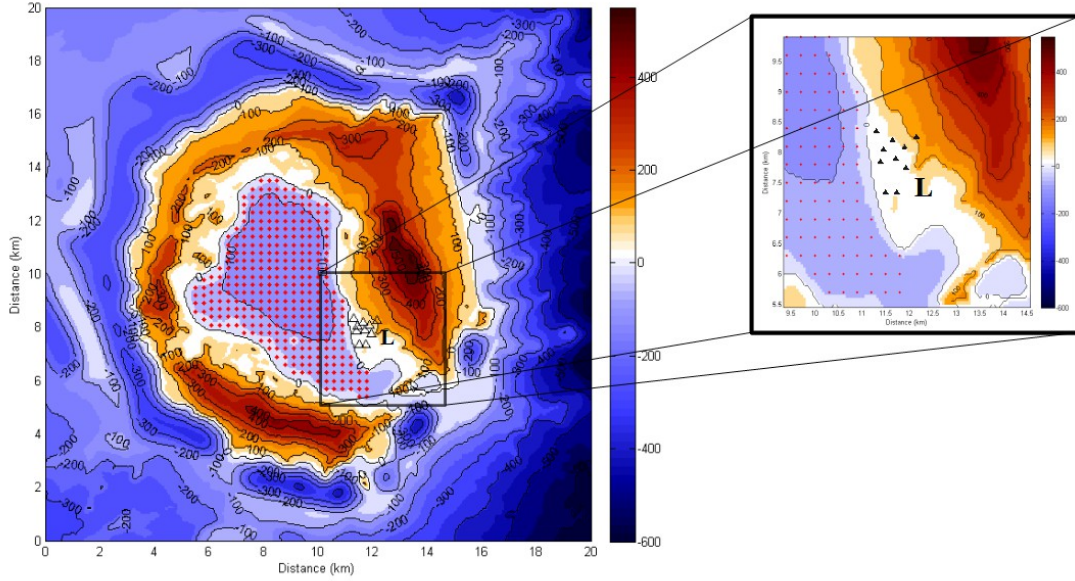
Figure 7. Distribution of shots within Port Foster and location of array L on its eastern shore. The original positions of the array stations needed to be adjusted in order to fit to the 50 m grid of the computational domain.

2009; Ben-Zvi *et al.*, 2009). A large high velocity anomaly appears to the NW of the island, around the area which had already identified as the margin of the Bransfield Basin crust (Zandhomenegi *et al.*, 2009) and the most important source of regional seismicity.

The method described by Ohminato and Chouet (1997) points out that stable results are possible even when strong velocity contrasts are included within the computational domain. However, the original density, P-wave and S-wave velocity data only contained actual data from points at or beneath the topography/bathymetry, being the rest of the data interpolated to construct the aforementioned domain. Thus, to obtain a more accurate velocity model, the correct values of P-wave, S-wave and density had to be changed from their original interpolated values to 1500 m/s, 0 m/s and 1000 kg/m^3 respectively at those nodes located in the ocean (Figure 6c). To achieve this, a new piece of Matlab code was written in order to locate the exact nodes that needed to be modified and apply the said changes (see Appendix 2). The cells above the free surface still contained wave velocity data due to the initial interpolation process, but it was not necessary to apply any change to them because the software automatically sets the Lamé coefficients set to 0 for all of them in order to ignore their effect on the wave propagation.

4.1.2. Parameters.
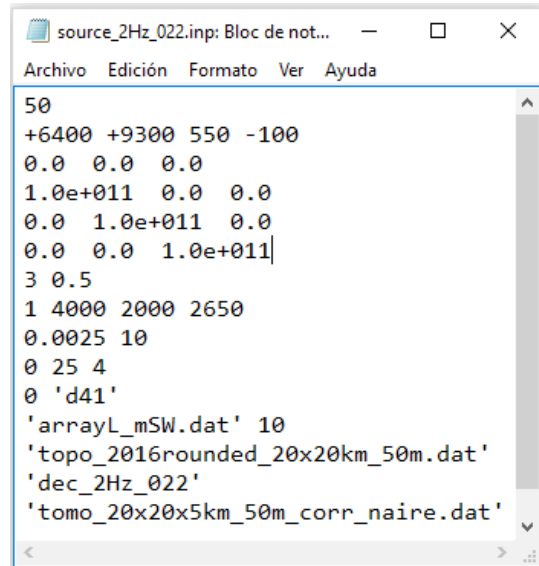
The finite-difference method requires two essential conditions to be satisfied. The first one establishes that a certain number of grids per wavelength are necessary for stable computation and avoidance of any numerical artifacts. In their work, Ohminato and Chouet (1997) establish 25 grids per wavelength as the optimum grid size, but they also clarify that it can vary depending on the geometry of the problem and mention that 15 grids per wavelength is enough in some cases. Here, with a grid size of 50 metres, the more restrictive condition (25 grids per wavelength) sets a maximum wavelength of

1250 metres. Now, if we consider that frequency, wave velocity and wavelength are related through $f = v/\lambda$, then, by considering the lowest wave velocity to expect in our model (1500 m/s), this condition sets 1.2 Hz as an upper limit to the frequency of the sources. However, if we only take 15 grids per wavelength, it is possible to simulate sources with frequencies up to 2 Hz. The spectra of the original explosions were centred at 6 Hz, so ideally the synthetic sources should have as high a frequency as possible. For this reason, two different series of simulations were carried on as part of this work. The original sources used for TOMODEC experiment were air gun shots located close to the sea surface. Those explosions created acoustic waves that travelled through the water and, eventually, hit the sea floor, generating seismic waves in the process. The synthetic counterparts of the original shots are 331 isotropic point sources with cosine time functions with frequencies of 1 and 2 Hz seconds respectively, all of them located on the surface of the sea floor within Port Foster (which ranges in depth from 50 to 150 m in our model) on a 300 m grid (Figure 7). They are numbered from 1 to 331 starting from South to North and West to East. García Yeguas et al. (2011) studied eight different seismic arrays. For this work, we focused just on array L, located on the southeastern coast of Port Foster. The experimental results for this array show important propagation anomalies, both in terms of anomaly magnitude (up to 60 degrees in azimuth) and extension. Thus it is a good candidate for our test.

This method also imposes a condition to the time step in order to ensure that the derivatives can be replaced by the finite differences (Ohminato and Chouet, 1997; Alford *et al.*, 1974; Virieux and Madariaga, 1982; Chouet, 1986; Clayton and Engquist, 1977). This condition is written as $\Delta t < (\Delta h \cdot (0.8)^2)/\sqrt{3}\alpha$, being Δh the grid interval, and α the P-wave velocity. Thus, by considering only the largest P-wave velocity (6858 m/s), this condition sets 2.6 ms as the threshold to the time step. Here, it was finally set to 2.5 ms.

The finite-difference method was applied by means of the *topo_v17* software provided by Dr. Javier Almendros (Ohminato and Chouet, 1997). This programme required the creation of a file with a set of input parameters for each shot (Figure 8), specifically:

- Cell dimensions: 50 m.

- Spatial coordinates of the explosions: the horizontal coordinates were defined from the southwestern corner of the domain, while the sea level was the reference for elevation (both in metres).

- Position of the synthetic stations: also defined from the southwestern corner of the domain (in metres).

- Maximum elevation within the

```
50
+6400 +9300 550 -100
0.0   0.0   0.0
1.0e+011   0.0   0.0
0.0   1.0e+011   0.0
0.0   0.0   1.0e+011
3 0.5
1 4000 2000 2650
0.0025 10
0 25 4
0 'd41'
'arrayL_mSW.dat' 10
'topo_2016rounded_20x20km_50m.dat'
'dec_2Hz_022'
'tomo_20x20x5km_50m_corr_naire.dat'
```

Figure 8. Snapshot of one of the input files containing all the required parameters for the topo_v17 software. Appendix 3, at the end of this document, contains a piece of Matlab code which was used to create the 662 parameter files required for the finite-difference method, as well as a run file calling each file in turn to be read.

domain: 550 m.

- Moment tensor components: isotropic explosions have diagonal moment tensors with diagonal components equal to M_0, which was set to 10^{11} N·m in this case.

- Force: as isotropic explosions do not produce any net acceleration over the source, all three components of the force were set to zero.

- Time step: 0.0025 s. From this parameter it is possible to obtain the effective sampling interval of the seismograms, as only 1 out of 4 samples are taken to create them, thus setting it to 0.01 s.

-Seismogram length: there are big differences in source-to-array distances, being some of them even more than 5 km away from it. Thus, the seismograms needed to be long enough to allow all signals to reach the receivers but not as long as to allow any possible reflection created at the borders of the domain to come across the array. After all these considerations, it was set to 10 seconds.

- Modified topographic and tomographic data files.

The application of this programme produced a series of array files (one for each shot) containing the 10 seconds long seismograms registered at each station of the array. Optionally, the software produces a set of displacement snapshots which visually show the propagation of the wavefield for each shot. As Appendix 5 shows, two new different Matlab routines, containing some functions provided by Dr. Javier Almendros, allowed: 1) the separation of each signal into an individual *sac* file, thus obtaining 3310 seismogram files for each series of simulations (1 Hz and 2 Hz); and 2) the addition of 10 seconds of flat signal at the beginning of the synthetic seismograms. The analysis of these seismograms by means of the zero lag cross-correlation method requires the creation of a time window that is then shifted along the seismogram (see next section for details about ZLCC method). For those sources located near the array, the first arrival of the seismic waves is quite immediate, thus making it more difficult to analyse it. Therefore, the addition of several seconds of flat signal improves the recognition of the first arrival of the seismic waves during the next phase of the analysis. Finally, synthetic noise (filtered white noise) was also added to each signal to make it more similar to actual seismograms and avoid numerical indeterminations while applying the ZLCC method (this process is also explained in Appendix 5).

4.2. Zero lag cross-correlation method.

The resulting array data were analysed by using the *cc8mre_sac* software (also provided by Dr. Javier Almendros, which calculates the apparent slowness and the azimuth of the first arrivals in the synthetic seismograms by using the Zero Lag Cross Correlation (ZLCC) method (Frankel *et al.* 1991; Del Pezzo *et al.* 1997; Almendros *et al.* 1999). It consists on evaluating every possible value of the apparent slowness within a grid in order to maximize the average cross-correlation coefficient. The application of this method implies the assumption of a homogeneous medium below the array, a wavefield composed only of plane waves and the random character of the noise, which would make null its correlation with the signal. The different distances from each

station to the source leads to travel time differences, given by

$$\tau_{jk} = t_k - t_j = \mathbf{s}(\mathbf{r}_k - \mathbf{r}_j) = -s((x_k - x_j)\sin\alpha + (y_k - y_j)\cos\alpha) \quad,$$

where t_j and t_k are the arrival times for stations j and k respectively, $\mathbf{r}_j$ and $\mathbf{r}_k$ are their respective positions, $\mathbf{s}$ is the slowness vector, s is the apparent slowness and α is the back-azimuth. The known positions of the stations allows for an estimation of the delay in the signal arrivals, τ_{jk}, and, therefore, the determination of the slowness vector by minimizing

$$\sum_{j,k=1}^{N} (\tau_{jk}' - \mathbf{s} \cdot (\mathbf{r}_k - \mathbf{r}_j))^2$$

The cross-correlation coefficient, is defined as

$$c_{jk}(\tau_{nm}) = \langle u_j(t+t_m) u_k(t+t_n) \rangle \quad,$$

u_j and u_k being the seismograms of stations j and k respectively. Thus, its maximum value corresponds to τ_{jk} equalling the travel time difference between stations j and k. If all possible pairs of stations are taken into account, the average cross-correlation coefficient is given by

$$C = \frac{1}{N^2} \frac{\sum_{j,k=1}^{N} c_{jk} \cdot (\tau_{jk})}{\sqrt{(c_{jj}(0)c_{kk}(0))}}$$

As before, a series of parameters need to be defined in order to apply this method to the synthetic data which was previously obtained from the finite-difference method, like maximum apparent slowness, time window length, position of the array stations, etc. The maximum expected apparent slowness can be obtained from the empirical dispersion curves for Rayleigh waves obtained by Luzón et al. (2010) for the same eight arrays deployed for the TOMODEC experiment. They show that, at array L, surface waves move with a phase velocity of approximately 0.75 km/s for 1 Hz and nearly 0.5 km/s for 2 Hz waves. Since surface waves are the slowest, this sets a limit to the maximum apparent slowness that can be detected with the array.

The whole set of parameters required for the ZLCC method is:

-Position of the array stations in kilometres.

-Length of the signals: 2001 samples.

-Time window length: this is an important though delicate parameter, as long windows allow for lower noise levels and short windows improve temporal resolution, but it has been suggested that, optimally, it should contain at least two cycles of the signal (Almendros *et al.*, 1999). Therefore, it was set to 200 samples for 1Hz sources and 100 samples for the 2Hz ones.

-Number of samples to skip at the start of the signal (300 in both cases) and number of windows (139 for 1 Hz and 298 for 2 Hz).

-Filtering frequencies were set to 0.4 to 3 Hz, a range approximately centred

at the sources' frequencies.

-Apparent slowness grid size and spacing: by inverting the results obtained by Luzón et al. (2010), we get 1.33 s/km for 1 Hz sources and 2 s/km for 2 Hz sources. Some initial tests showed that the relevant wave phases for this study moved with slownesses lower than 1.5 s/km and so the grid size was set to this value for both sets of sources; as for the spacing, the minimum grid interval can be estimated as the result of dividing the sampling interval by the array aperture, thus yielding an approximate result of 0.01 s/km.

Figure 9. Example of an input file containing all the required parameters for the cc8_mre_sac software. Appendix 4 contains a Matlab script describing how the 662 files were created and defining all parameters.

The *cc8mre_sac* programme requires all these parameters to be contained within a sequence of files (Figure 9), being the result of its application three time series of apparent slowness, back-azimuth and average cross-correlation coefficient with their respective uncertainties for each shot. The uncertainty of the solution depends strongly on the array configuration, as small arrays suffer from lower resolution and larger uncertainty due to the wide shape of the peaks within their response functions, while large arrays may be affected by spatial aliasing due to the superposition of peaks (Figure 10).

In order to assign a single value of each variable to each shot at each frequency, the obtained results were analysed with *arrayevents*, a Matlab routine provided by Dr. Javier Almendros (Almendros *et al.*, 2001, a, b) which allows the calculation of the average value of apparent slowness, back azimuth and correlation in a temporal window around the arrival of the selected phase, being it either the P-wave (first motion to be registered in the seismogram) or the surface waves (the most energetic wave phase)

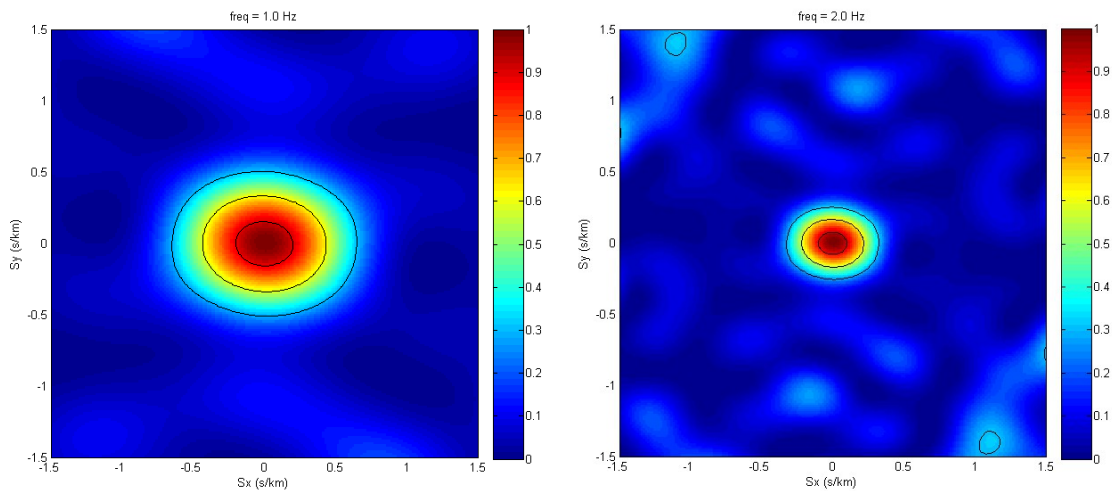*Figure 10. Array response functions for synthetic array L at 1 Hz (left) and 2 Hz (right). These functions depend only on the wave frequency and the number and position of the stations. Thus, large arrays like array L may show a single wide peak and, therefore, lower resolution at low frequencies (left) and narrower ones (better though possibly not unique solutions) at higher frequencies (right).*

a)

cc_2Hz_168.out | 11.23- 11.52 s | 6 windows
azi 309 [326] 349 deg | slo 0.20 [0.29] 0.39 s/km | ccmax 0.987

b)

cc_2Hz_168.out | 12.98- 13.78 s | 16 windows
azi 316 [324] 333 deg | slo 0.54 [0.63] 0.71 s/km | ccmax 0.976
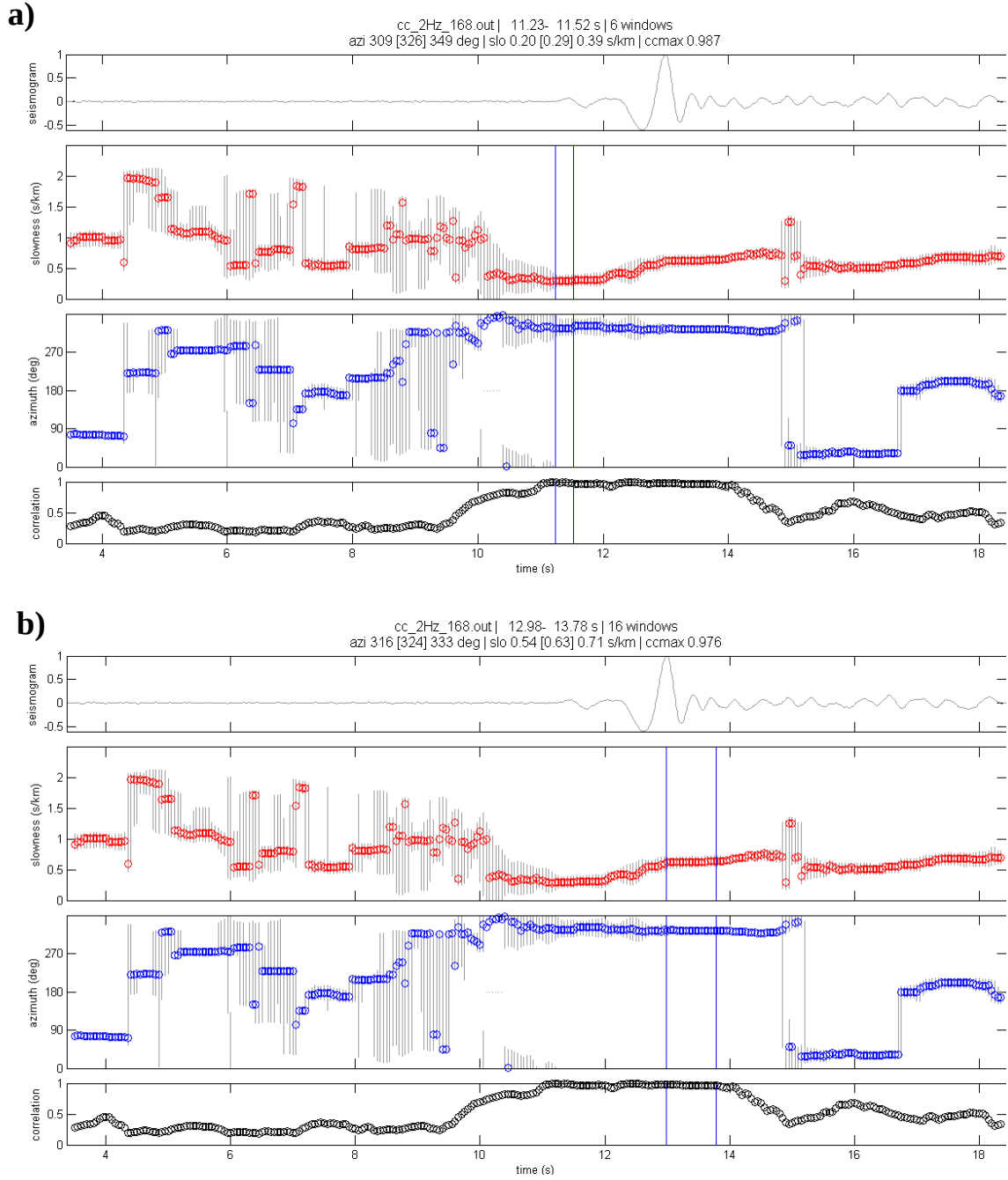
Figure 11. Display of the seismogram (top graph a and b) and apparent slowness, azimuth and cross correlation results(in red, blue and black respectively) for each time window. The grey bars indicate the uncertainty of each solution and the blue bars the selected solutions according to the aforementioned criteria in each case (see text for details).

(Figure 11), which are easily identifiable in the apparent slowness vector results. All solutions were selected according to the following criteria: 1) simultaneous occurrence of a correlation peak (at least higher than 0.8) and stable solutions with low uncertainties both in apparent slowness and azimuth values; 2) temporal proximity to the arrival of the wave phase. Figure 11 illustrates this procedure for a 2 Hz source when selecting the arrival of the P-wave (a) and surface waves (b). The solutions

between the blue bars correspond to those that satisfy the aforementioned criteria and the values of apparent slowness, azimuth and cross correlation are averaged within this interval and saved to an output file. It is convenient to note that the number of such solutions varies with source-to-array distance and frequency. Actually, for 1 Hz sources close to the array, the larger size of the time windows and the lower resolution made it impossible to separate the arrival of P-waves from that of surface waves, so in those cases both phases were picked together in order to obtain a unique value of apparent slowness, back azimuth and correlation.

5. Results and discussion.

The first step in the analysis of the resulting data was the observation of the evolution of waveforms with distance. Two sets of sources with north-south and east-west linear distributions were selected for that purpose (Figure 12). As all stations in the array registered similar signals, only seismograms and results from station 2 (marked with a black triangle on Figures 12 and 16) will be shown in this section.

The small amplitude of the first arrivals made it necessary to normalize the seismograms showed on figures 13, 15a and 17a to their respective P-waves maximum amplitude in order to be able to see them, even if it entailed the impossibility to properly observe any changes on the rest of the seismogram. Variations on surface waves are shown on figures 14, 15b and 17b, where data were normalized to their absolute maximum amplitude. As expected, seismograms for 1 Hz (Figure 13a) and 2 Hz (Figure 13b) sources show quite similar waveforms and evolution with distance. For the sake of simplicity, only 2 Hz seismograms are shown in figures 14 and 15, which illustrate waveform changes along the N-S profile for surface waves (Figure 14) and the E-W one both for P and surface waves (Figure 14).

As the sources were designed to resemble the original air-gun shots, the synthetic seismograms show the expected relatively impulsive first arrivals. Specifically, in
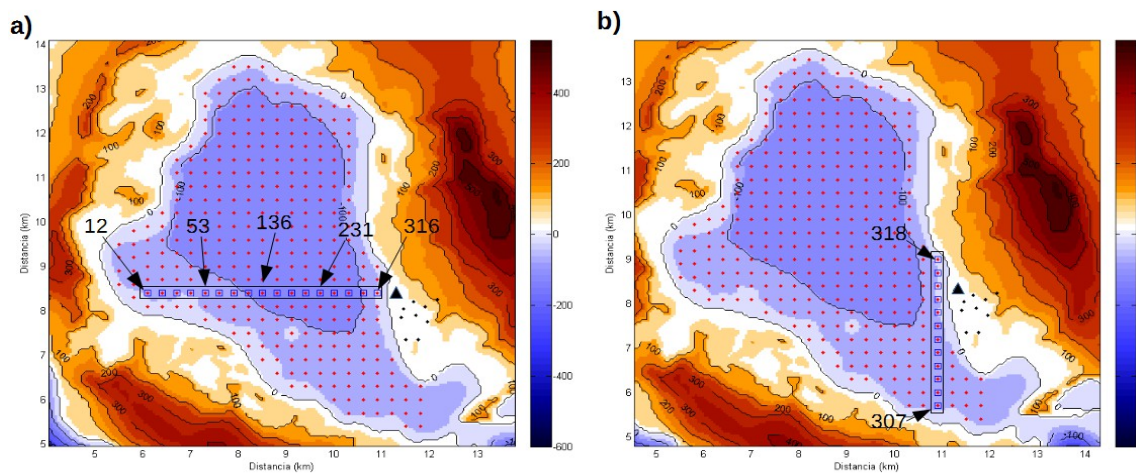

Figure 12. N-S and E-W profiles selected for the evaluation of waveform changes with shot-to-array distance. In (a), sources numbers go from 307 (bottom) to 318 (top), consecutively, while in (b), they go non-consecutively from 12 (left) to 316 (right) .
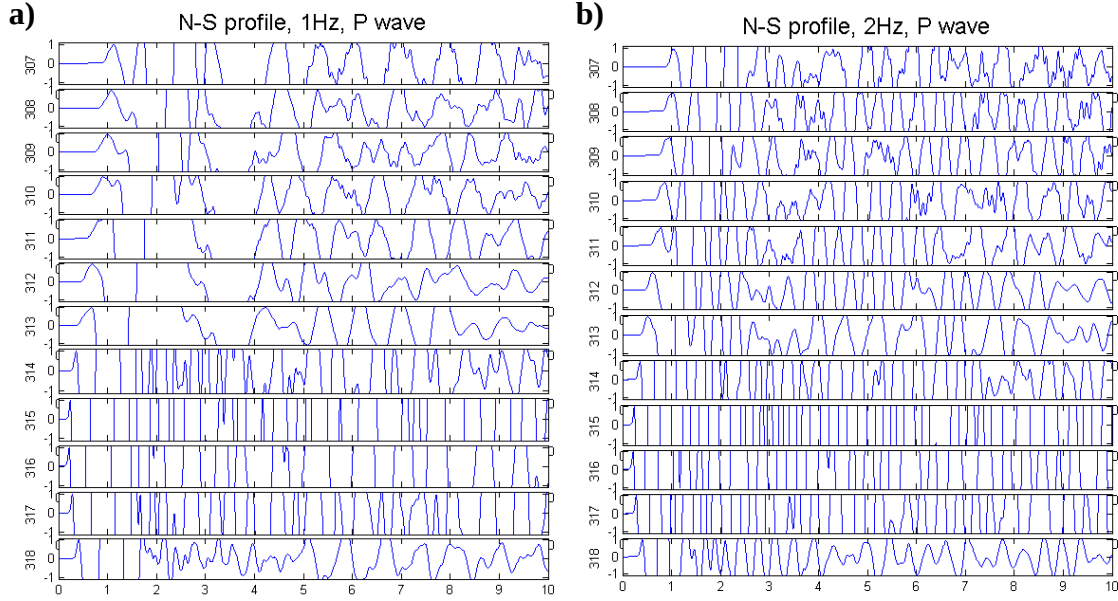
21

Figure 13. Seismograms for the stations located along the N-S profile for 1 Hz (a) and 2 Hz (b). In both cases, the signals were normalized to the maximum P-wave amplitude.

Figure 13, sources 316 and 307 are the closest and the farthest to the array, respectively, and it is possible to observe how the initial shape of the P-wave gets wider and even divides into two different peaks as source-to-array distance increases. However, besides the expected change in width, sources 307 to 313 show waveforms quite different from those of sources 314 to 318. Figure 14 shows that, besides the expected delayed arrival of surface waves to the farthest stations, it is possible to observe the same change in waveform which was already seen in figure 13. Thus, seismograms corresponding to sources along the N-S profile show a marked difference between the northernmost sources and the southernmost ones. Interestingly, sources 314 to 318 are located over a high velocity area (Figures 5 and 6c) while the rest lay over a low velocity one, thus offering a possible explanation for the observed differences and a reason to expect azimuth anomalies and differences in apparent slowness results in these areas.

The E-W profile, however, crosses the large low velocity area also showed by Zandomeneghi *et al.*, (2009). Waveforms along this profile (Figure 15) change slowly from west to east with some nearly isolated sources (like 279 or 316) showing very different seismograms, which could be due to the irregular shape of the low velocity area at different depths and the decreasing source-to-array distance. In figures 15a and 15b, it is possible to observe how waveforms change gradually from west to east from wider shapes to narrower ones. For example, sources 12 to 71 are quite similar to each other, as are sources
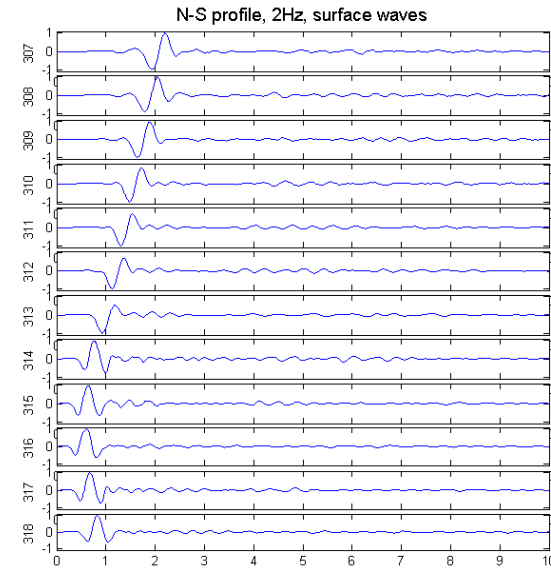

Figure 14. Seismograms for 2 Hz sources located along the north-south profile.

22

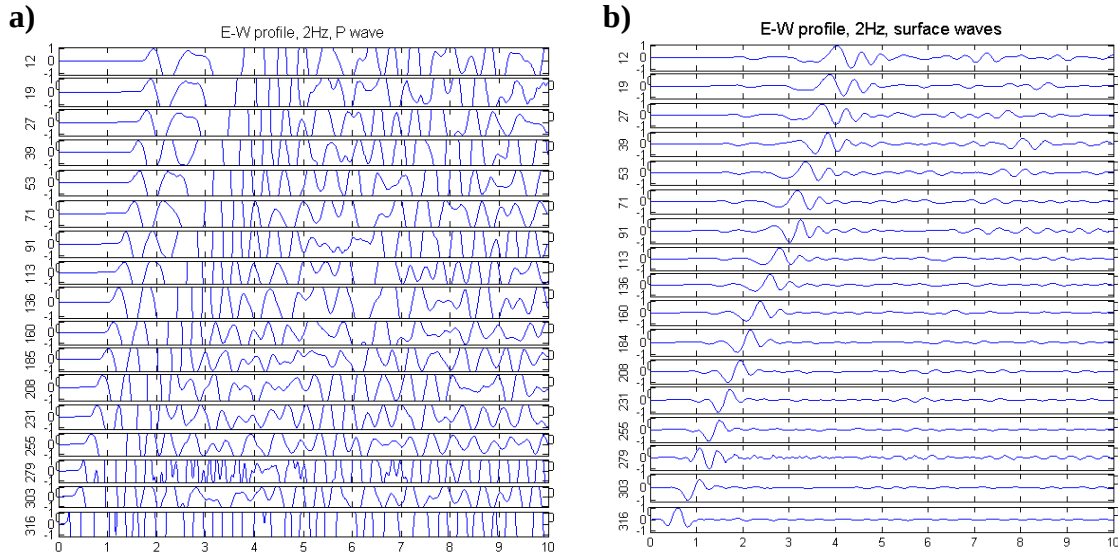a)   b)

Figure 15. Seismograms for all sources located along the east-west profile, conveniently normalized in order to improve the observation of first arrivals (a) and surface waves (b).

160 to 208, but there are also some which do not seem to fit in, like sources 91 and 303. Therefore, it is also to be expected to find differences in apparent slowness and/or azimuth results for those groups and particular sources.

Figures 13 to 15 show mainly the effect of distance (alongside topography and tomography) on the resulting waveforms, but García Yeguas *et al.* (2011), also mentioned observing some differences depending on the source azimuth. In order to look into those variations, 14 sources, all located approximately 2 km away from station 2, were selected (Figure 16, station 2 is marked with a black triangle) and their seismograms compared (Figure 17). Despite being located almost at the same distance, it is possible to observe some differences in their waveforms, specially when studying surface waves. In the case of P waves (Figure 17a), the first arrivals are nearly identical in all cases. However, it is possible to see important differences in the waveforms for sources 205, 227 and 250, located to the southwest of the arc on figure 16 (sources inside the black rectangle) right after that first impulse. The same distinction can be seen for surface waves, as waveforms for sources 205, 227 and 250 notably differ from the ones generated by the rest of the sources.

Figures 18 and 19 help illustrating these singularities. It has already been mentioned that the *topo_v17* software could also produce a series of snapshots representing the motion of the medium caused by the passing wavefronts. Specifically, the snapshots presented here
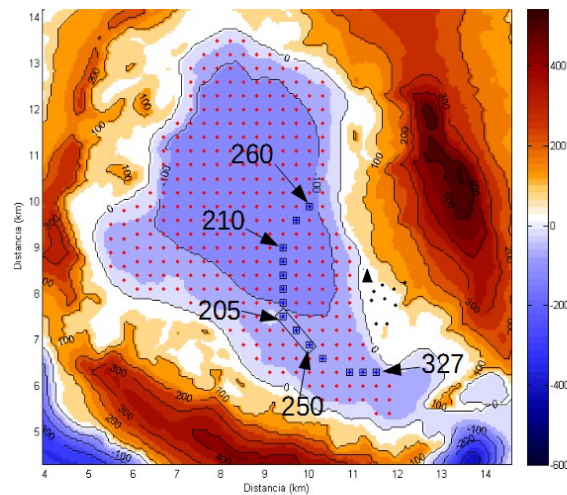

Figure 16. Selection of sources according to their distances to the northwesternmost station of array, which is highlighted in magenta. Sources numbers go from 205 to 327, non-consecutively, starting from left to right and bottom to top. Sources 205, 227 and 250 are those inside the black rectangle (see text for details).

23
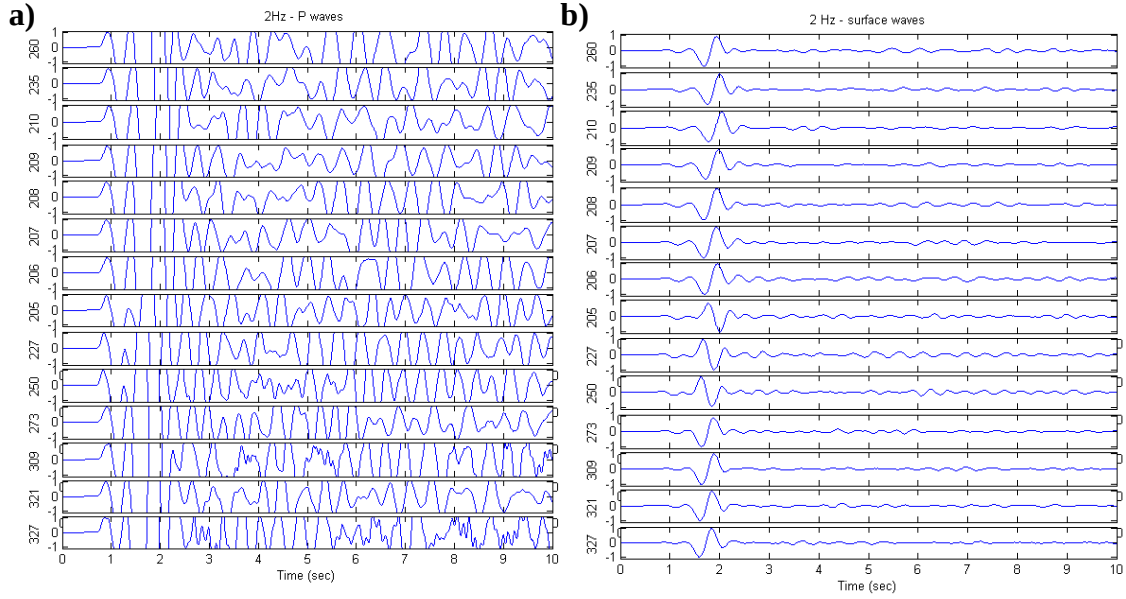
Figure 17. Seismograms registered for sources approximately 2 km away from the array. In order to make it easier to appreciate the differences in waveforms, as these sources are not numbered consecutively, here they are shown from source 260 (the one located most north on Figure 15) and then turning counterclockwisely.

illustrate only vertical motion, its magnitude given in μm by the color scale to the right of each figure. Matlab routines *snapsurf3* and *snapsurfmovie*, provided by Dr. Javier Almendros, allow the visualization of such snapshots.

Thus, Figure 18 contains two snapshots taken 2.25 s after the explosions of 2 Hz sources 205 and 206, which are only 300 m distant from each other (Figure 16). However, at this time, the wavefronts being registered at station 2 (the black triangle on the eastern shore of Port Foster) are quite different. For source 206 (Figure 18a), the first vibrations to arrive to station 2 move upwards (positive values) before taking it down (wide yellow-orange-red band). The magnitude of the first vibrations to reach station 2 is approximately 0.2 μm. At 2.25 s, at the location of station 2, the motion is
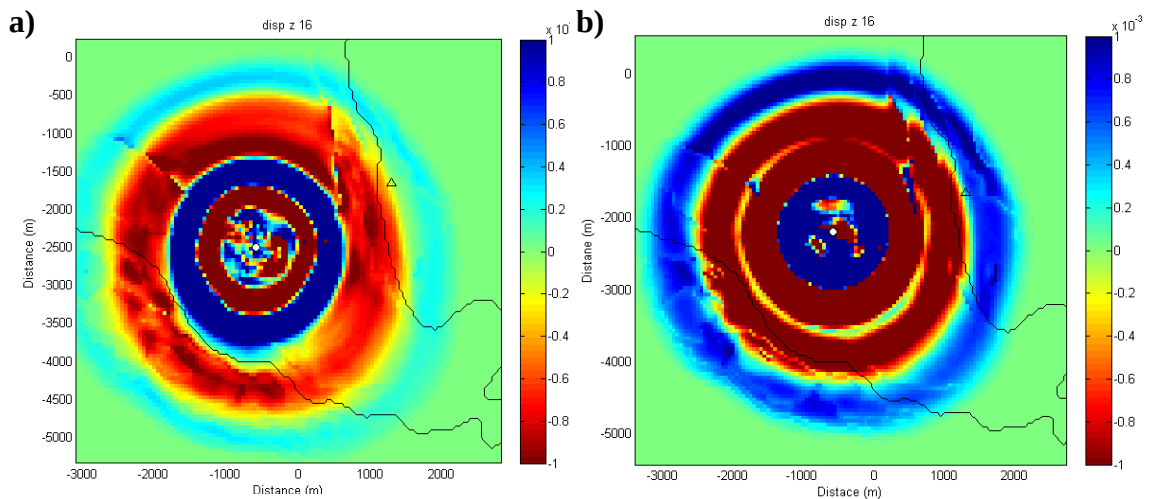
Figure 18. Snapshots representing the first wavefronts to reach station 2 for adjacent 2 Hz sources 206 (a) and 205 (b), taken 2.25 s after the synthetic explosions. The colour scale to the right represents the magnitude of the vibrations/movement (in mm) caused by the acoustic waves.

24

Figure 19. Representation of the arrival of the wavefronts generated by sources 250 (a) and 273 (b) to stations 2. The vertical movement of the ground is given by the colour bar to the right (in mm).

negative (-0.3 μm approx.). For source 205 (Figure 18b), however, the movement goes directly upwards and reaches its maximum magnitude (around 1 μm) just before going quickly down to its minimum (-1 μm approx.).
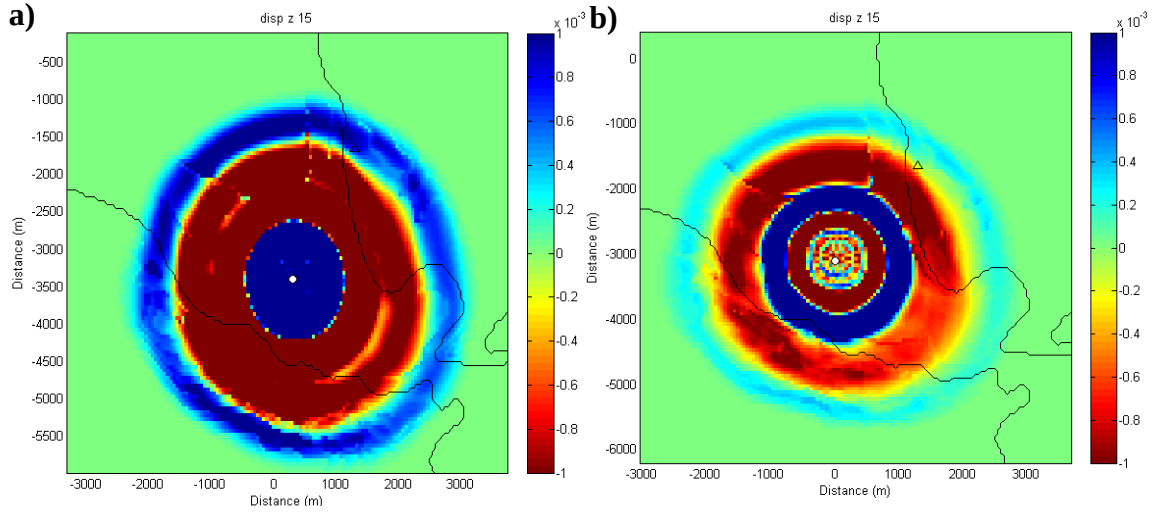
Something similar happens in the case of sources 250 and 273, which are 424.3 m away from each other. In this case, the snapshots presented on Figure 19 were taken 1.88 s after the synthetic explosion. The resemblance between snapshots from sources 250 and 205, and 206 and 273 is quite clear, even if the distance between these sources is greater than between the ones being compared here. Again, the magnitude of the movement at 1.88 s at station 2 is positive (nearly 1 μm) for source 250, while it is negative (approximately -0.3 μm) for source 273.

The results shown in previous figures point to those areas where it should be more likely to find differences in azimuth or apparent slowness. *Arrayanomaly*, a piece of software provided by Dr. Javier Almendros, allows to represent azimuth anomaly and apparent slowness results over Port Foster map (Figures 20 to 24). For each shot, the apparent slowness and azimuth anomaly results obtained from the ZLCC method at the array site are assigned to the shot location and then an interpolation process calculates the anomaly values for the rest of Port Foster.

Figure 20 shows the azimuth anomaly results for 1 and 2 Hz sources respectively, comparing those results obtained from P-wave detection data and those from surface waves data. In all four cases the distribution of the anomaly seems to be quite the same. A large positive anomaly area appears to the north of Port Foster, with azimuth anomaly magnitude reaching 20 degrees (this meaning a 20 degrees clockwise rotation of the apparent slowness vector from the shot-array direction). Another positive anomaly area to the southeast of the bay is also present in all these graphs, its magnitude much lower than that of the large one. The small negative anomaly area in the vicinity of the array is also a common feature, with up to 30 degrees apparent slowness vectors counterclockwise rotations. The main difference among these azimuth anomaly distributions is the more "detailed" distribution obtained for 2 Hz sources, which indicates a stronger effect of the topography and velocity structure over their
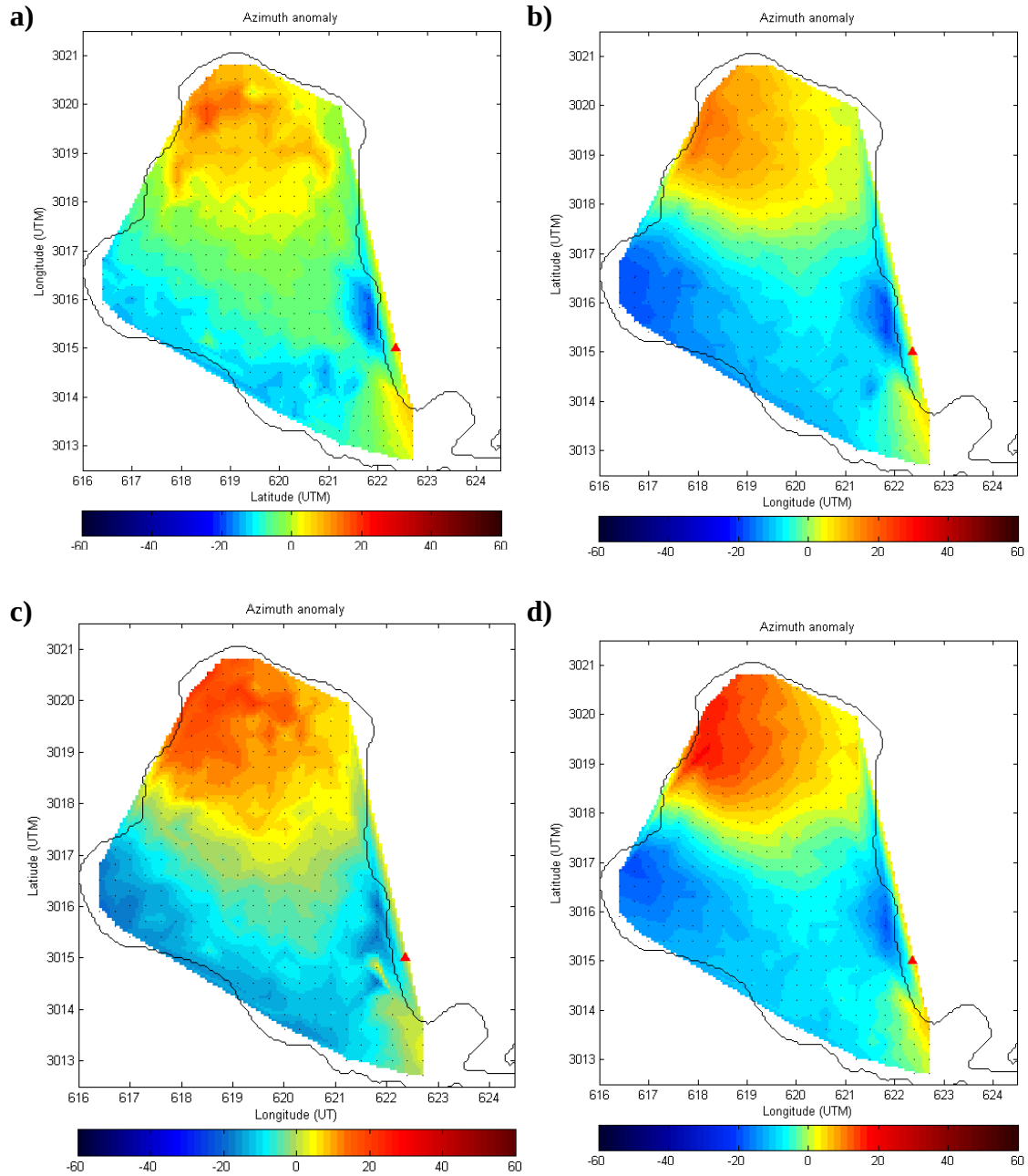
Figure 20. Azimuth anomaly distribution for 1 Hz (a and b) and 2Hz sources (c and d). Graphs a and c contain the results obtained from P-wave data, while b and d show those from surface waves data.

propagation than over the 1 Hz ones.

Figure 21 is analogue to Figure 20, but for slowness. It compares the results obtained for 1 and 2 Hz sources and P-wave and surface waves data. However, these distributions are not as similar among them as the azimuth anomaly ones were. Again, 2 Hz sources show more variations of apparent slowness (therefore, a greater effect of the topography and velocity structure) than the 1 Hz ones, but the remaining distribution seems to coincide in all four graphs except for the apparent slowness magnitude, which is naturally higher for surface waves as they move slower than P-waves. For 1 Hz sources, there seems to be some kind of artifact around the position of the southern end
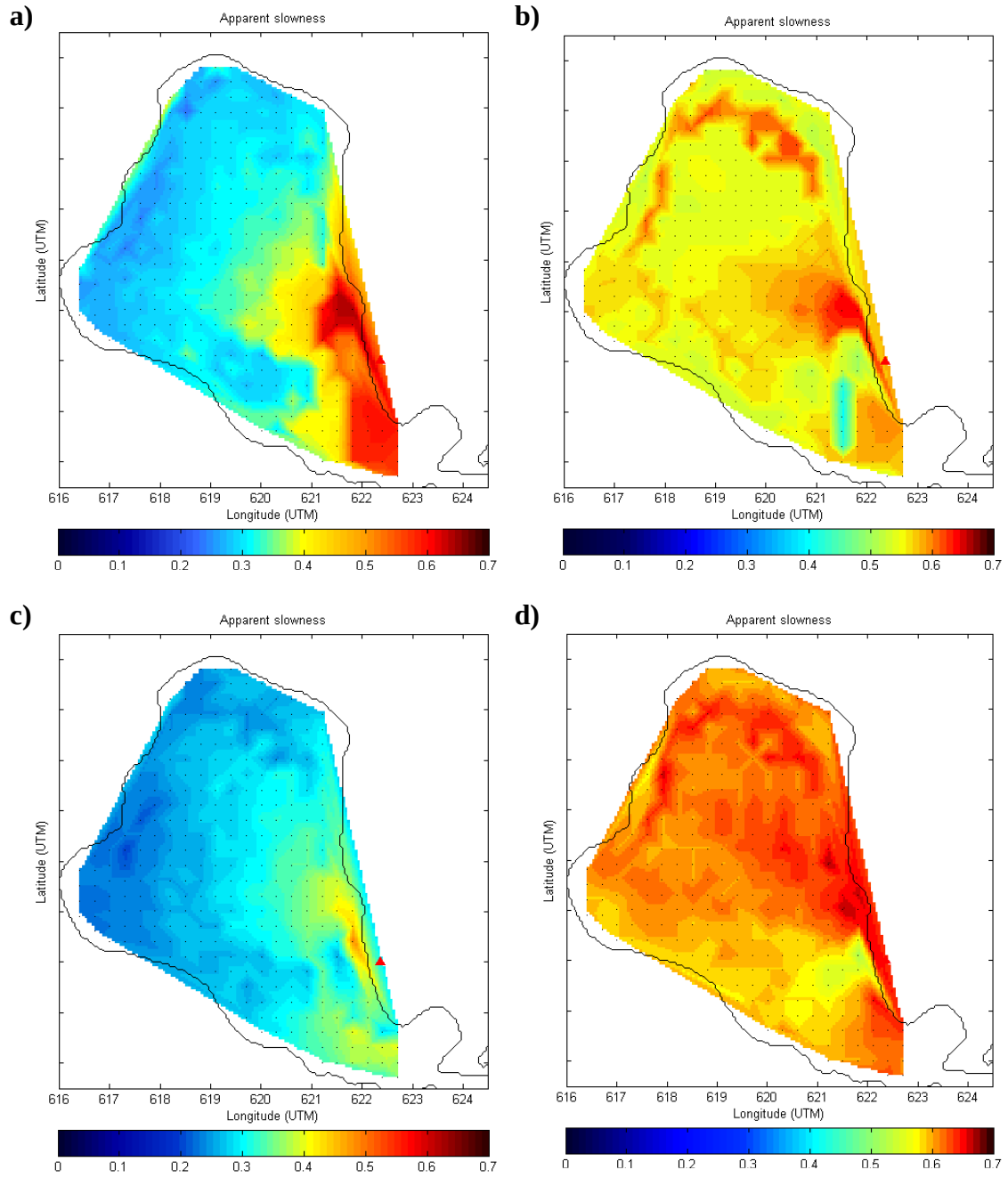
Figure 21. Apparent slowness distributions for 1 Hz (a and b) and 2 Hz (c and d) sources. As in Figure 20, left graphs (a and c) show the results for P-wave, while the right ones contain those for surface waves (c and d). Note that different color scales have been used for P-wave and surface waves graphs in order to facilitate the visualization of variations in the apparent slowness magnitude.

of the north-south profile used on Figure 12, both for P-wave and surface waves. As it has already been explained in section 4.2., it was not possible to separate the arrival of P-waves from that of surface waves for these sources, therefore the abnormal distribution and magnitude of apparent slowness in this area.

| García Yeguas *et al.* (2011) | 2 Hz, P wave |
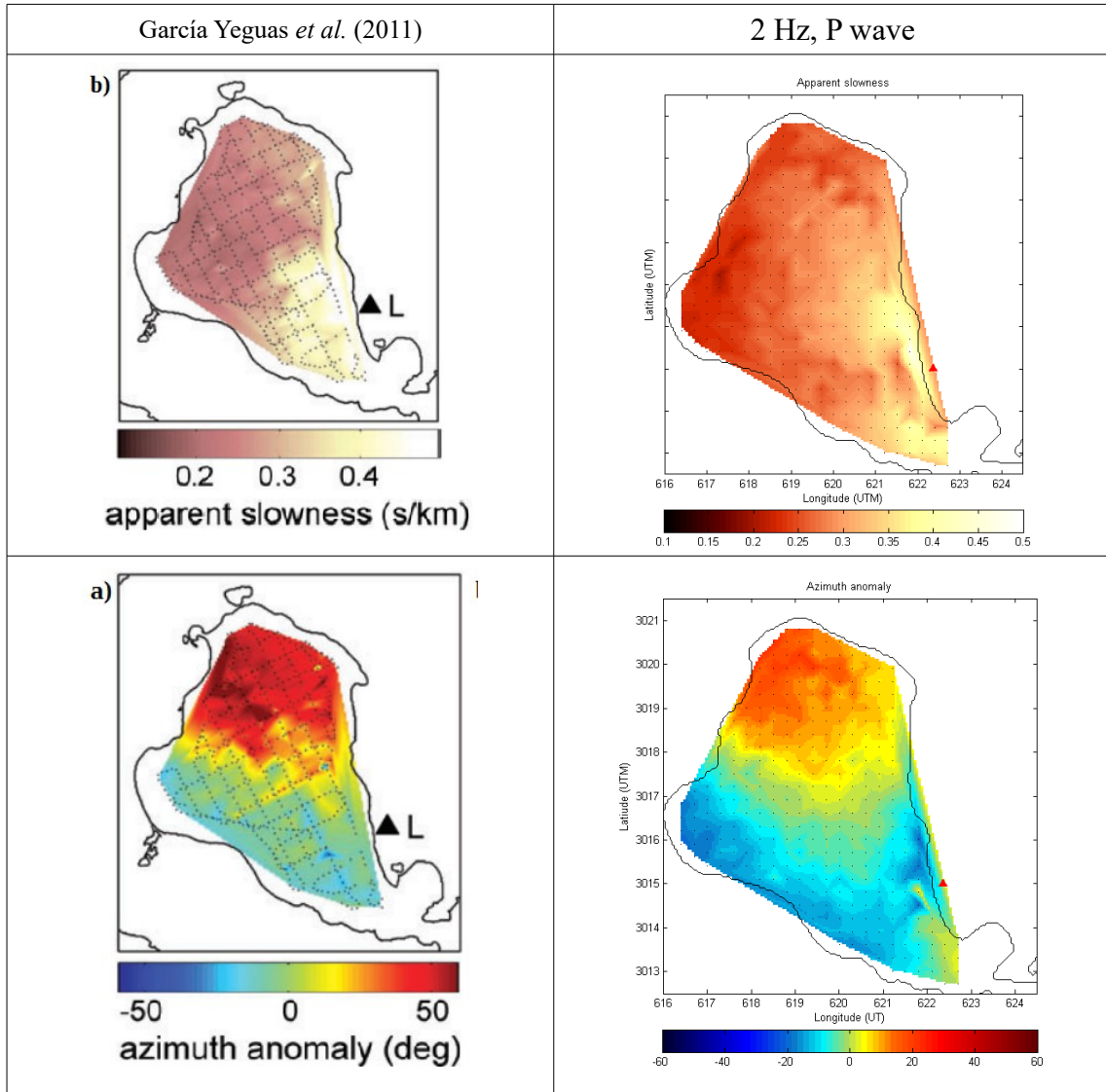
Figure 22. *On the left, graphical display of García Yeguas et al. (2011) apparent slowness and azimuth anomaly data. Synthetic results are shown on the right for 2 Hz sources. Both colormap and scale have been set to resemble the original diagrams and make comparisons easier.*

As this study has tried to replicate the results obtained by García Yeguas et al. (2011), a final comparison between experimental and synthetic apparent slowness and azimuth anomaly results is required. In order to facilitate it, Figure 22 displays the original results by García Yeguas *et al.* (2011) for P-wave azimuth anomaly and apparent slowness next to the same results obtained for 2 Hz sources from these simulations. The colour map has been changed here in order to make both graphs look as similar as possible.

Apparent slowness results show great similarity with García Yeguas *et al.* (2011) data, both in distribution and magnitude. Some of the observed singularities on these figures could also be explained by observing Figures 5 and 6. In the case of sources 205, 227 and 250, for example, tomography data show a transition from a low velocity area to a high velocity one around the position of sources 205, 227 and 250. Lower

values of apparent slowness appear around northwestern Port Foster, thus agreeing both with experimental and tomographic data, as this is where the low velocity region was located (Figures 5 and 6c). Nearby shots, however, produce larger apparent slowness values, especially those located around the high velocity area to the south of the array. Comparing these maps with the seismograms showed on figures 13, 14, 15 and 17, it is possible to see a correlation between the observed differences and singularities along the different profiles and the changes in apparent slowness shown on figure 22. Along the E-W profile, there are several small regions with different values of apparent slowness that approximately coincide with the positions of the sources showing changes in their seismograms. As for the N-S profile, the northern sources show higher apparent slowness values, while the southernmost ones produced slightly lower ones. This result also coincides with the observed changes in the seismograms showed on Figure 13b and 14. Sources 205, 227 and 250 (see Figure 16 for location) also seem to be placed over a region with lower apparent slowness than its surroundings, thus showing a correlation with our previous observations.
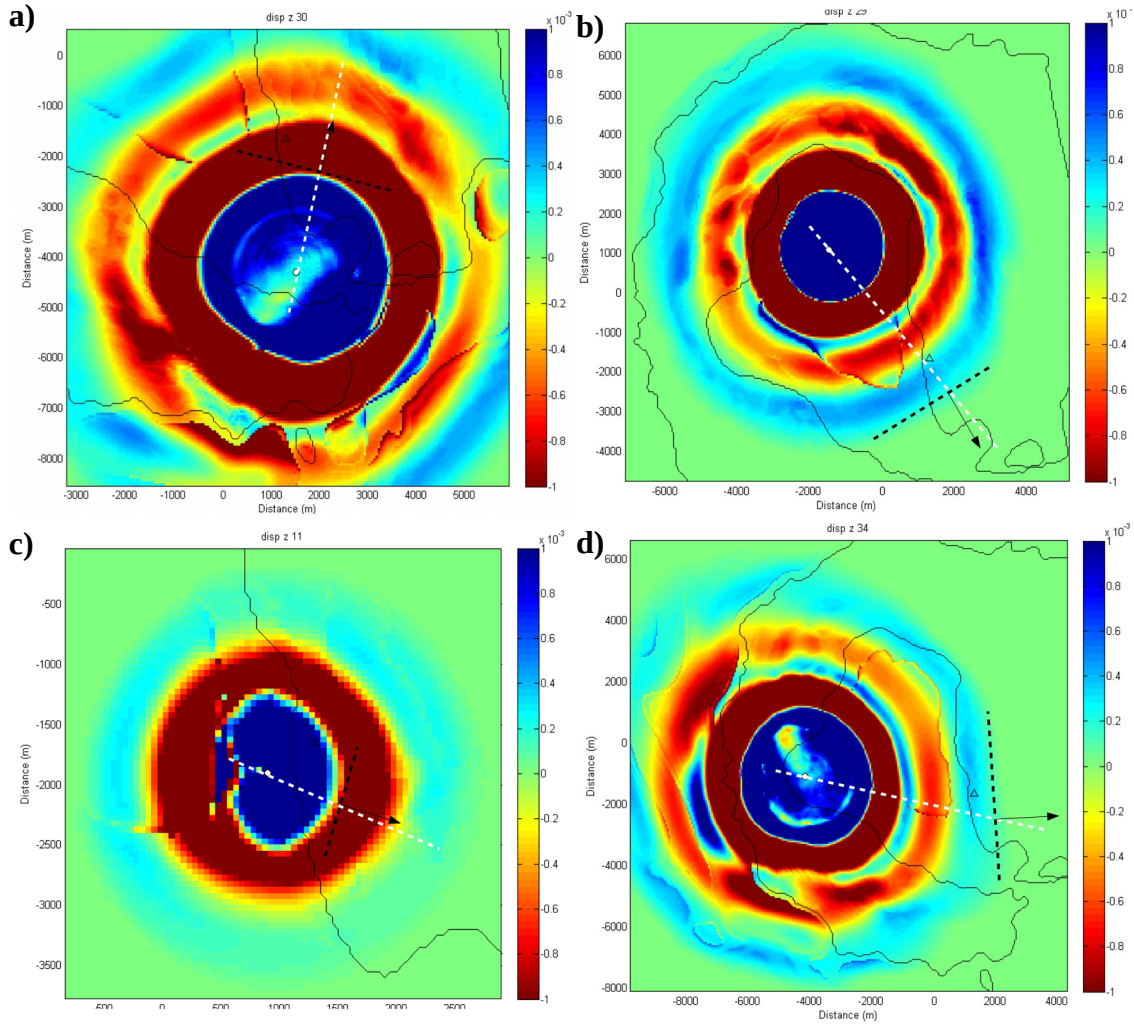
Figure 24. Snapshots showing the wavefront propagation for four different sources. Source (a) is located above the high velocity area to the south of the array. Source (b), however, is places right in the middle of the large low velocity area to the North of Port Foster. Sources (c) and (d) are among the closest (c) and farthest (d) to the array, thus helping observing the effect of distance on wave propagation. As in previous cases, the colour scale to the right quantifies the vertical motion of the ground in millimetres.

Azimuth anomaly results are also very similar to the experimental ones. The large positive azimuth anomaly region to the north of Port Foster (meaning that rays with origin within this region deviate from the source-to-array direction clockwise) seem to be located right above the low velocity area (Figures 5 and 6c) while the negative anomaly region on southwestern Port Foster seem to indicate that seismic rays travel around the hypothesised magma chamber (thus being deviated counterclockwise from the path they would follow on a homogeneous medium) on their way to the array. Again, the observed differences along the profiles coincide with marked differences on azimuth anomalies. Sources on the northern end of the N-S profile show large negative azimuth anomalies (up to 30-40 degrees) while those towards the southern end of the profile show much lower anomalies. Along the E-W profile, azimuth anomaly values range from small negative values to nearly 20 degrees in irregular distributions, thus agreeing with the observed changes in the seismograms. However, there do not seem to be big differences in azimuth anomaly among the sources on Figure 16.

Finally, Figure 24 contains snapshots from four different sources located at interesting locations. These figures show illustrating the observed irregularities in wave propagation. In an ideal, homogeneous medium, the wavefronts would be perfectly round and symmetric, while the apparent slowness vectors would point in the source-to-array direction. In all these figures, the white dashed line represents the shot-to-array direction (to the center of the array), while the black dashed line is a tangent to the wavefront. As apparent slowness vectors are perpendicular to the propagation direction (thus, to the wavefront tangent), the black arrows represent the azimuth of apparent slowness vectors at those locations.

Source (a) is located over the right velocity area to the south of the array. This snapshot was taken 3.75 s after the explosion and it shows how irregular the wavefronts are (the wide yellow-red wavefront is nearly square and the pale blue one is almost a semicircle). At the array site, the apparent slowness vector appears to be very slightly rotated clockwise from the shot-to-array direction, thus coinciding with the small but positive azimuth anomaly already found for this source. Source (b), on the other hand, is placed near the centre of the large low velocity area to the North of Port Foster. Again, it is possible to appreciate some distortion in the wavefront shapes, with the apparent slowness vector appearing turned clockwise again, as expected from this source. As for sources (c) and (d), they are the closer to the array and one of the farthest ones respectively. As in previous cases, the wavefronts do not look symmetric, even at such short distances as in figure 24c. The apparent slowness vectors are rotated counterclockwise in both cases, thus agreeing with previous results which showed negative azimuth anomalies in these areas.

6. Conclusions and future work.

Volcanic environments are very heterogeneous and their topography is usually very sharp. These factors have been traditionally neglected in order to apply simpler calculation methods but it is necessary (and possible) to consider more realistic mediums if we want to fully understand volcanic seismicity and dynamics.

In their work, García Yeguas *et al.* (2011) found important wave propagation anomalies which were hypothesised as the result of topography and velocity structure. In this work, a realistic domain including both the velocity structure of Deception Island and its topography (both of them acknowledging the presence of the ocean around the island) was applied for our simulations. Apparent slowness vectors results can vary greatly depending on even small variations of the position of the source, thus the importance of using an accurate velocity model for array studies.

The limitations of our method and the resolution of both the topography and tomography data did not allow to recreate the original sources more accurately, as only frequencies up to 2 Hz were possible and the original sources had spectra centred at 6 Hz. Furthermore, the analysis of sources located near the array showed some problems, especially at low frequencies. One of the requirements of the ZLCC method was that the wavefield would be composed by plane waves only. However, for sources near the array, the curvature of the wavefronts can not be ignored and may have produced the observed anomalous results. Still, the obtained distributions of apparent slowness and azimuth anomaly within Port Foster coincide greatly with those of García Yeguas *et al.* (2011), thus demonstrating that their results were produced by a combined effect of the topography and the velocity structure. It is also convenient to note that seismic waves generated by higher frequency sources are more affected by sharp topographies and heterogeneities than those with lower frequencies, thus implying that the observed differences between the results on figure 22 and those of García Yeguas *et al.* (2011) could be due to differences between the frequency content of their respective sources. Moreover, it would be reasonable to expect even more similar results by using synthetic sources with higher frequencies.

These results prove the accuracy and usefulness of numeric simulations. As they allow to approximately predict the results, they can help planning experiments like the one carried out at Deception Island.

It would be useful to be able to separate the effects of topography from those due to the velocity structure of the area. A whole new series of simulations could be carried on using a completely homogeneous medium and the same topography used here and another one considering only the velocity structure over a flat medium, thus obtaining the apparent slowness and azimuth anomaly distributions caused by these feature on their own.

Another interesting study would be that of the rest of the seismic arrays analysed by García Yeguas et al. (2001). From this work, we know how the topography and velocity structure affect the seismic waves received at array L. The work by García Yeguas et al. (2011) comprised six different seismic arrays located all around Port Foster. Their results not only showed wave propagation anomalies, but also important differences among the different arrays. Therefore, repeating these simulations for each of those arrays would improve the knowledge about Deception Island volcano.

References

Abril, M., (2007): " Evolución, diseño y desarrollo de antenas sísmicas. Las antenas del Gran Sasso, del Vesubio y las nuevas antenas sísmicas portátiles del Instituto Andaluz de Geofísica. Aplicación a zonas tectónicas y volcánicas", Tesis Doctoral, Universidad de Granada, España.

Alford, R. M., Kelly, K. R., & Boore, D. M. (1974). Accuracy of finite-difference modeling of the acoustic wave equation. *Geophysics*, *39*(6), 834-842.

Alguacil, G., Almendros, J. C., Del Pezzo, E., Garcia, A., Ibañez, J. M., La Rocca, M., ... & Ortiz, R. (1999). Observations of volcanic earthquakes and tremor at Deception Island-Antarctica. *Annals of Geophysics*, *42*(3).

Almendros, J., Ibáñez, J. M., Alguacil, G., Del Pezzo, E., & Ortiz, R. (1997). Array tracking of the volcanic tremor source at Deception Island, Antarctica. *Geophysical Research Letters*, *24*(23), 3069-3072.

Almendros, J., Ibáñez, J. M., Alguacil, G., & Del Pezzo, E. (1999). Array analysis using circular-wave-front geometry: an application to locate the nearby seismo-volcanic source. *Geophysical Journal International*, *136*(1), 159-170.

Almendros, J., Chouet, B., & Dawson, P. (2001a). Spatial extent of a hydrothermal system at Kilauea Volcano, Hawaii, determined from array analyses of shallow long-period seismicity. I- Method. *Journal of Geophysical Research*, *106*(B7), 13565-13580.

Almendros, J., Chouet, B., & Dawson, P. (2001b). Spatial extent of a hydrothermal system at Kilauea Volcano, Hawaii, determined from array analyses of shallow long-period seismicity. II- Results. *Journal of Geophysical Research*, *106*(B7), 13581-13597.

Alparone, S., Cannata, A., & Gresta, S. (2007). Time variation of spectral and wavefield features of volcanic tremor at Mt. Etna (January–June 1999). *Journal of volcanology and geothermal research*, *161*(4), 318-332.

Baker, P. E. (1969). Volcanic activity at Deception Island in 1967 and 1969. *Nature*, *224*, 553-560.

Baker, P. E., McReath, I., Harvey, M. R., Roobol, M. J., & Davies, T. G. (1975). *The geology of the South Shetland islands: V. Volcanic evolution of Deception island* (Vol. 78). British Antarctic Survey.

Barclay, A. H., Wilcock, W. S. D., & Ibáñez, J. M. (2009). Bathymetric constraints on the tectonic and volcanic evolution of Deception Island Volcano, South Shetland Islands. *Antarctic Science*, *21*(02), 153-167.

Bartolini, S., Geyer, A., Martí, J., Pedrazzi, D., & Aguirre-Díaz, G. (2014). Volcanic hazard on Deception Island (South Shetland Islands, Antarctica). *Journal of Volcanology and Geothermal Research*, *285*, 150-168.

Bean, C. J., De Barros, L., Lokmer, I., Métaxian, J. P., O'Brien, G., & Murphy, S. (2014). Long-period seismicity in the shallow volcanic edifice formed from slow-rupture earthquakes. *Nature Geoscience*, *7*(1), 71-75.

Benz, H. M., Chouet, B. A., Dawson, P. B., Lahr, J. C., Page, R. A., & Hole, J. A. (1996). Three-dimensional P and S wave velocity structure of Redoubt Volcano, Alaska.

Journal of Geophysical Research: Solid Earth, *101*(B4), 8111-8128.

Ben-Zvi, T., Wilcock, W. S., Barclay, A. H., Zandomeneghi, D., Ibáñez, J. M., & Almendros, J. (2009). The P-wave velocity structure of Deception Island, Antarctica, from two-dimensional seismic tomography. *Journal of Volcanology and Geothermal Research*, *180*(1), 67-80.

Cannata, A., Catania, A., Alparone, S., & Gresta, S. (2008). Volcanic tremor at Mt. Etna: Inferences on magma dynamics during effusive and explosive activity. *Journal of Volcanology and Geothermal Research*, *178*(1), 19-31.

Cannata, A., Giudice, G., Gurrieri, S., Montalto, P., Alparone, S., Di Grazia, G., ... & Liuzzo, M. (2009). Relationship between soil CO_2 flux and volcanic tremor at Mt. Etna: implications for magma dynamics, Environ. *Earth Sci*, *61*, 477-489.

Carmona, E., Almendros, J., Serrano, I., Stich, D., & Ibáñez, J. M. (2012). Results of seismic monitoring surveys of Deception Island volcano, Antarctica, from 1999–2011. *Antarctic Science*, *24*(05), 485-499.

Chouet, B. (1986). Dynamics of a fluid-driven crack in three dimensions by the finite difference method. *Journal of Geophysical Research: Solid Earth*, *91*(B14), 13967-13992.

Chouet, B. A. (1996). Long-period volcano seismicity: its source and use in eruption forecasting. *Nature*, *380*(6572), 309-316.

Chouet, B. A. (1996). New methods and future trends in seismological volcano monitoring. In *Monitoring and mitigation of volcano hazards* (pp. 23-97). Springer Berlin Heidelberg.

Chouet, B., Dawson, P., Ohminato, T., Martini, M., Saccorotti, G., Giudicepietro, F., ... & Scarpa, R. (2003). Source mechanisms of explosions at Stromboli Volcano, Italy, determined from moment-tensor inversions of very-long-period data. *Journal of Geophysical Research: Solid Earth*, *108*(B1).

Christeson, G. L., Barker, D. H., Austin, J. A., & Dalziel, I. W. (2003). Deep crustal structure of Bransfield Strait: Initiation of a back arc basin by rift reactivation and propagation. *Journal of Geophysical Research: Solid Earth*, *108*(B10).

Clayton, R., & Engquist, B. (1977). Absorbing boundary conditions for acoustic and elastic wave equations. *Bulletin of the seismological society of America*, *67*(6), 1529-1540.

Cooper, A. P. R., Smellie, J. L., & Maylin, J. (1998). Evidence for shallowing and uplift from bathymetric records of Deception Island, Antarctica. *Antarctic Science*, *10*(04), 455-461.

Cruz, F. G., & Chouet, B. A. (1997). Long-period events, the most characteristic seismicity accompanying the emplacement and extrusion of a lava dome in Galeras Volcano, Colombia, in 1991. *Journal of Volcanology and Geothermal Research*, *77*(1), 121-158.

Dawson, P. B., Chouet, B. A., Okubo, P. G., Villaseñor, A., & Benz, H. M. (1999). Three-dimensional velocity structure of the Kilauea Caldera, Hawaii. *Geophysical Research Letters*, *26*(18), 2805-2808.

Del Pezzo, E., La Rocca, M., & Ibanez, J. (1997). Observations of high-frequency

scattered waves using dense arrays at Teide volcano. *Bulletin of the Seismological Society of America*, *87*(6), 1637-1647.

De Luca, G., Scarpa, R., Del Pezzo, E., & Simini, M. (1997). Shallow structure of Mt. Vesuvius volcano, Italy, from seismic array analysis. *Geophysical Research Letters*, *24*(4), 481-484.

De Rosa, R., Mazzuoli, R., Omarini, R. H., Ventura, G., & Viramonte, J. G. (1995). A volcanological model for the historical eruptions at Deception Island (Bransfield Strait, Antarctica). *Terra Antartica*, *2*(2), 95-101.

Dietrich, R., Dach, R., Engelhardt, G., Ihde, J., Korth, W., Kutterer, H. J., ... & Müller, C. (2001). ITRF coordinates and plate velocities from repeated GPS campaigns in Antarctica–an analysis based on different individual solutions. *Journal of Geodesy*, *74*(11-12), 756-766.

Di Grazia, G., Falsaperla, S., & Langer, H. (2006). Volcanic tremor location during the 2004 Mount Etna lava effusion. *Geophysical research letters*, *33*(4).

Di Grazia, G., Cannata, A., Montalto, P., Patanè, D., Privitera, E., Zuccarello, L., & Boschi, E. (2009). A multiparameter approach to volcano monitoring based on 4D analyses of seismo-volcanic and acoustic signals: The 2008 Mt. Etna eruption. *Geophysical Research Letters*, *36*(18).

Fehler, M. (1983). Observations of volcanic tremor at Mount St. Helens volcano. *Journal of Geophysical Research: Solid Earth*, *88*(B4), 3476-3484.

Fernandez-Ibanez, F., Perez-Lopez, R., Martinez-Diaz, J. J., Paredes, C., Giner-Robles, J. L., Caselli, A. T., & Ibanez, J. M. (2005). Costa Recta beach, Deception Island, West Antarctica: a retreated scarp of a submarine fault?. *Antarctic Science*, *17*(03), 418-426.

Frankel, A., Hough, S., Friberg, P., & Busby, R. (1991). Observations of Loma Prieta aftershocks from a dense array in Sunnyvale, California. *Bulletin of the seismological Society of America*, *81*(5), 1900-1922.

Galindo-Zaldívar, J., Jabaloy, A., Maldonado, A., & De Galdeano, C. S. (1996). Continental fragmentation along the South Scotia Ridge transcurrent plate boundary (NE Antarctic Peninsula). *Tectonophysics*, *258*(1), 275-301.

García Yeguas, A., Almendros, J., Abella, R., & Ibáñez, J. M. (2011). Quantitative analysis of seismic wave propagation anomalies in azimuth and apparent slowness at Deception Island volcano (Antarctica) using seismic arrays. *Geophysical Journal International*, *184*(2), 801-815.

Goldstein, P., Chouet, B., 1994. Array measurements and modelling of a source of shallow volcanic tremor at Kilauea Volcano, Hawaii. *J. Geophys. Res.* 99, 2637– 2652.

González-Ferrán, O. (1995). *Volcanes de Chile*. Instituto Geográfico Militar.

González-Ferrán, O., Katsui, Y., & Tavera, J. (1970). *Contribución al conocimiento geológico de la Península Byers, de la Isla Livingston; Islas Shetland del Sur, Antártica*. Universidad de Chile, Facultad de Ciencias Físicas y Matemáticas.

Gresta, S., Montalto, A., & Patane, G. (1991). Volcanic tremor at Mount Etna (January 1984–March 1985): its relationship to the eruptive activity and modelling of the summit feeding system. *Bulletin of volcanology*, *53*(4), 309-320.

Hagerty, M. T., Schwartz, S. Y., Garces, M. A., & Protti, M. (2000). Analysis of seismic and acoustic observations at Arenal Volcano, Costa Rica, 1995–1997. *Journal of Volcanology and Geothermal Research*, *101*(1), 27-65.

Hawkes, D. D. (1961). The geology of the South Shetland Islands: II. The geology and petrology of Deception Island.

Ibáñez, J. M., Carmona, E., Almendros, J., Saccorotti, G., Del Pezzo, E., Abril, M., & Ortiz, R. (2003). The 1998–1999 seismic series at Deception Island volcano, Antarctica. *Journal of volcanology and geothermal research*, *128*(1), 65-88.

Keller, R. A., Fisk, M. R., Smellie, J. L., Strelin, J. A., & Lawver, L. A. (2002). Geochemistry of back arc basin volcanism in Bransfield Strait, Antarctica: Subducted contributions and along-axis variations. *Journal of Geophysical Research: Solid Earth*, *107*(B8).

Klepeis, K. A., & Lawver, L. A. (1996). Tectonics of the Antarctic-Scotia plate boundary near Elephant and Clarence Islands, West Antarctica. *Journal of Geophysical Research: Solid Earth*, *101*(B9), 20211-20231.

Koulakov, I., Yudistira, T., & Luehr, B. G. (2009). P, S velocity and VP/VS ratio beneath the Toba caldera complex (Northern Sumatra) from local earthquake tomography. *Geophysical Journal International*, *177*(3), 1121-1139.

Kumagai, H., & Chouet, B. A. (1999). The complex frequencies of long-period seismic events as probes of fluid composition beneath volcanoes. *Geophysical Journal International*, *138*(2), F7-F12.

Lahr, J. C., Chouet, B. A., Stephens, C. D., Power, J. A., & Page, R. A. (1994). Earthquake classification, location, and error analysis in a volcanic environment: Implications for the magmatic system of the 1989–1990 eruptions at Redoubt Volcano, Alaska. *Journal of Volcanology and Geothermal Research*, *62*(1), 137-151.

Lawver, L. A., Sloan, B. J., Barker, D. H., Ghidella, M., Von Herzen, R. P., Keller, R. A., ... & Chin, C. S. (1996). Distributed, active extension in Bransfield Basin, Antarctic Peninsula: evidence from multibeam bathymetry. *GSA Today*, *6*(11), 1-6.

Lombardo, G., Coco, G., Corrao, M., & Gresta, S. (1996). Features of seismic events and volcanic tremor during the preliminary stages of the 1991-1993 eruption of Mt. Etna. *Annals of Geophysics*, *39*(2).

Lopes, Fernando C., et al. "The development of the Deception Island volcano caldera under control of the Bransfield Basin sinistral strike-slip tectonic regime (NW Antarctica)." *Geological Society, London, Special Publications* 401.1 (2015): 173-184.

López-Martínez, J., Smellie, J.L., Thomson, J.W., Thomson, *Geology and geomorphology of Deception Island. M.R.A. (eds.). Cambridge, British Antarctic Survey, 77 pp. (2002).*

Luo, Y., & Schuster, G. (1990). Parsimonious staggered grid finite-differencing of the wave equation. *Geophysical Research Letters*, *17*(2), 155-158.

Maestro, A., Somoza, L., Rey, J., Martínez-Frías, J., & López-Martínez, J. (2007). Active tectonics, fault patterns, and stress field of Deception Island: a response to oblique convergence between the Pacific and Antarctic plates. *Journal of South American Earth Sciences*, *23*(2), 256-268.

Martí, J., Vila, J., & Rey, J. (1996). Deception Island (Bransfield Strait, Antarctica): an example of a volcanic caldera developed by extensional tectonics. *Geological Society, London, Special Publications*, *110*(1), 253-265.

Martí, J., Geyer, A., & Aguirre-Diaz, G. (2013). Origin and evolution of the Deception island caldera (South Shetland Islands, Antarctica). *Bulletin of volcanology*, *75*(6), 1-18.

Maurice, R., Stacey, D., Wiens, D. A., Shore, P. J., Vera, E., & Dorman, L. M. (2003). Seismicity and tectonics of the South Shetland Islands and Bransfield Strait from a regional broadband seismograph deployment. *Journal of Geophysical Research: Solid Earth*, *108*(B10).

McNutt, S. R. (2002). 25 Volcano seismology and monitoring for eruptions. *International Geophysics*, *81*, 383-V.

McNutt, S. R. (2005). Volcanic seismology. *Annu. Rev. Earth Planet. Sci.*, *32*, 461-491.

Monteiller, V., Got, J. L., Virieux, J., & Okubo, P. (2005). An efficient algorithm for double-difference tomography and location in heterogeneous media, with an application to the Kilauea Volcano. *Journal of Geophysical Research: Solid Earth*, *110*(B12).

Moser, T. J. (1991). Shortest path calculation of seismic rays. *Geophysics*, *56*(1), 59-67.

Neuberg, J. (2000). Characteristics and causes of shallow seismicity in andesite volcanoes. *Philosophical Transactions of the Royal Society of London A: Mathematical, Physical and Engineering Sciences*, *358*(1770), 1533-1546.

Newhall, C. A., & Dzurisin, D. (1989). Historical unrest at large calderas of the world. *Journal of Geology; (USA)*, *97*(5).

Ohminato, T., & Chouet, B. A. (1997). A free-surface boundary condition for including 3D topography in the finite-difference method. *Bulletin of the Seismological Society of America*, *87*(2), 494-515.

Ortiz, R., Vila, J., García, A., Camacho, A. G., Diez, J. L., Aparicio, A., ... & Petrinovic, I. (1992). Geophysical features of Deception Island. *Recent Progress in Antarctic Earth Science*, 443-448.

Ortiz, R., García, A., Aparicio, A., Blanco, I., Felpeto, A., Del Rey, R., ... & Olmedillas, J. C. (1997). Monitoring of the volcanic activity of Deception Island, South Shetland Islands, Antarctica (1986–1995). *The Antarctic Region: Geological Evolution and Processes*, 1071-1076.

Pallàs, R., Smellie, J. L., Casas, J. M., & Calvet, J. (2001). Using tephrochronology to date temperate ice: correlation between ice tephras on Livingston Island and eruptive units on Deception Island volcano (South Shetland Islands, Antarctica). *The Holocene*, *11*(2), 149-160.

Paredes, C., Pérez-López, R., Giner-Robles, J.L., de la Vega, R., García-García, A. & Gumiel, P. (2006). Spatial distribution of morpholineaments and tectonic zoning in the Deception Island (South Shetland, Antarctica), *Geogaceta*, 37, 75-78.

Park, J., Morgan, J. K., Zelt, C. A., Okubo, P. G., Peters, L., & Benesh, N. (2007). Comparative velocity structure of active Hawaiian volcanoes from 3-D onshore–offshore seismic tomography. *Earth and Planetary Science Letters*, *259*(3), 500-516.

Patane, D., Chiarabba, C., Cocina, O., De Gori, P., Moretti, M., & Boschi, E. (2002).

Tomographic images and 3D earthquake locations of the seismic swarm preceding the 2001 Mt. Etna eruption: evidence for a dyke intrusion. *Geophysical Research Letters*, *29*(10).

Patanè, D., Barberi, G., Cocina, O., De Gori, P., & Chiarabba, C. (2006). Time-resolved seismic tomography detects magma intrusions at Mount Etna. *Science*, *313*(5788), 821-823.

Patanè, D., Di Grazia, G., Cannata, A., Montalto, P., & Boschi, E. (2008). Shallow magma pathway geometry at Mt. Etna volcano. *Geochemistry, Geophysics, Geosystems*, *9*(12).

Patanè, D., Aiuppa, A., Aloisi, M., Behncke, B., Cannata, A., Coltelli, M., ... & Salerno, G. (2013). Insights into magma and fluid transfer at Mount Etna by a multiparametric approach: a model of the events leading to the 2011 eruptive cycle. *Journal of Geophysical Research: Solid Earth*, *118*(7), 3519-3539.

Pelayo, A. M., & Wiens, D. A. (1989). Seismotectonics and relative plate motions in the Scotia Sea region. *Journal of Geophysical Research: Solid Earth*, *94*(B6), 7293-7320.

Rey, J., Somoza, L., & Martínez-Frías, J. (1995). Tectonic, volcanic, and hydrothermal event sequence on Deception Island (Antarctica). *Geo-Marine Letters*, *15*(1), 1-8.

Roman, D. C., & Cashman, K. V. (2006). The origin of volcano-tectonic earthquake swarms. *Geology*, *34*(6), 457-460.

Saccorotti, G., Chouet, B., Martini, M., & Scarpa, R. (1998). Bayesian statistics applied to the location of the source of explosions at Stromboli Volcano, Italy. *Bulletin of the Seismological Society of America*, *88*(5), 1099-1111.

Saccorotti, G., Zuccarello, L., Del Pezzo, E., Ibanez, J., & Gresta, S. (2004). Quantitative analysis of the tremor wavefield at Etna Volcano, Italy. *Journal of volcanology and geothermal research*, *136*(3), 223-245.

Simkin, T., and L. Siebert (2002). *Global Volcanism Program*, Smithsonian Inst., Washington D.C.

Smellie, J. L. (1988). Recent observations on the volcanic history of Deception Island, South Shetland Islands. *British Antarctic Survey Bulletin*, (81), 83.

Smellie, J. L. (1989, July). Deception Island. In *Tectonics of the Scotia Arc, Antarctica. 28th International Geological Congress, Field Trip Guidebook* (Vol. 180, pp. 146-153).

Smellie, J. L. (1990). D. Graham Land and South Shetland Islands. *Volcanoes of the Antarctic plate and Southern oceans*, 302-359.

Smellie, J. L. (2001). Lithostratigraphy and volcanic evolution of Deception Island, South Shetland Islands. *Antarctic Science*, *13*(02), 188-209.

Stich, D., Almendros, J., Jiménez, V., Mancilla, F., & Carmona, E. (2011). Ocean noise triggering of rhythmic long period events at Deception Island volcano. *Geophysical Research Letters*, *38*(22).

Toomey, D. R., Solomon, S. C., & Purdy, G. M. (1994). Tomographic imaging of the shallow crustal structure of the East Pacific Rise at 9 30′ N. *Journal of Geophysical Research: Solid Earth*, *99*(B12), 24135-24157.

Valencio, D. A., Mendía, J., & Vilas, J. F. (1979). Palaeomagnetism and KAr age of

Mesozoic and Cenozoic igneous rocks from Antarctica. *Earth and Planetary Science Letters*, *45*(1), 61-68.

Vanorio, T., Virieux, J., Capuano, P., & Russo, G. (2005). Three‑dimensional seismic tomography from P wave and S wave microearthquake travel times and rock physics characterization of the Campi Flegrei Caldera. *Journal of Geophysical Research: Solid Earth*, *110*(B3).

Vila, J., Marti, J., Ortiz, R., Garcia, A., & Correig, A. M. (1992). Volcanic tremors at Deception Island (South Shetland Islands, Antarctica). *Journal of Volcanology and Geothermal Research*, *53*(1-4), 89-102.

Virieux, J. (1984). SH-wave propagation in heterogeneous media: Velocity-stress finite-difference method. *Geophysics*, *49*(11), 1933-1942.

Virieux, Jean. "P-SV wave propagation in heterogeneous media: Velocity-stress finite-difference method." *Geophysics* 51.4 (1986): 889-901.

Virieux, J., & Madariaga, R. (1982). Dynamic faulting studied by a finite difference method. *Bulletin of the Seismological Society of America*, *72*(2), 345-369.

Vuan, A., Maurice, S. R., Wiens, D. A., & Panza, G. F. (2005). Crustal and upper mantle S-wave velocity structure beneath the Bransfield Strait (West Antarctica) from regional surface wave tomography. *Tectonophysics*, *397*(3), 241-259.

Walker, G. P. (1984). Downsag calderas, ring faults, caldera sizes, and incremental caldera growth. *Journal of Geophysical Research: Solid Earth*, *89*(B10), 8407-8416.

White, R. A., Miller, A. D., Lynch, L., & Power, J. (1998). Observations of hybrid seismic events at Soufriere Hills volcano, Montserrat: July 1995 to September 1996. *Geophysical Research Letters*, *25*(19), 3657-3660.

García Yeguas, A., Almendros, J., Abella, R., & Ibáñez, J. M. (2011). Quantitative analysis of seismic wave propagation anomalies in azimuth and apparent slowness at Deception Island volcano (Antarctica) using seismic arrays. *Geophysical Journal International*, *184*(2), 801-815.

Zandomeneghi, D., Barclay, A., Almendros, J., Ibáñez Godoy, J. M., Wilcock, W. S., & Ben‑Zvi, T. (2009). Crustal structure of Deception Island volcano from P wave seismic tomography: Tectonic and volcanic implications. *Journal of Geophysical Research: Solid Earth*, *114*(B6).

Appendixes

All Matlab scripts listed here were written specifically for this work by the author.

Appendix 1

```matlab
%% DECEPTION ISLAND'S TOPOGRAPHY+BATHYMETRY %%


% The data file contains only one column with 160801 numbers,
% all of them representing the elevation of depth of every node
% of the grid (positive values for those over sea level and ne-
% matrix in order to visualize it.

cd('P:\Universidad\TFM\Datos')

%Load data:
topo=load('topodec2016_20x20km_50m.dat');
topo_rounded=load('topodec2016rounded_20x20km_50m_nocab.dat');%Rounded
to fit the 50m grid

%Create matrix:
topobat=reshape(topo,401,401);%topobat=topobat';
topobat_50m=reshape(topo_rounded,401,401);%topobat_50m=topobat_50m';

%Distance vectors (I place the origin at the center of the domain):
x=(-10000:50:10000);y=(-1)*(-10000:50:10000);

%UTM distance vectors:
xutm0=610904;ytum0=3007311;%In metres
x2=(0:50:20000);y2=(0:50:20000);
xutm=(xutm0+x2);yutm=(ytum0+y2);

%Station coordinates (in kilometres):
stts=load('arrayL_kmSW.dat');
%In metres:
stats=(stts*1000-10000);xstat=stats(:,1);ystat=stats(:,2);

%Array centre:
xmin=min(xstat);xmax=max(xstat);ymin=min(ystat);ymax=max(ystat);
x0=(xmin+xmax)/2;y0=(ymin+ymax)/2;


%% Topography and bathymetry separation  %%
%I need only topography information.

topovec=topo_rounded;

p=401;

for i=1:length(topovec)
    %I turn every negative value into zero:
```

```matlab
    if topovec(i)<0
        topovec(i)=0;
    end
end

solo_topo=[];

for n=0:400
    %Definition of topography matrix:
    solo_topo (n+1,:)=topovec(p*n+1:p*(n+1),:);
end

%Rename the variable for future plots:
topobat=topobat_50m;

%Save variables:
save('topomats.mat','x','y','topobat_50m','topobat','solo_topo','xstat
','ystat','x0','y0','xutm','yutm')

%Save data file:
filename='topo_2016rounded_20x20km_50m_nocab.dat';
dlmwrite(filename,topovec,'delimiter',' ','newline','unix')


%% TOPOGRAPHY AND BATHYMETRY REPRESENTATION %%

clear all
load topomats
solo_topo=load('topo_2016rounded_20x20km_50m_nocab.dat');
solo_topo=reshape(solo_topo,401,401);

% Plot elevation/depth lines at 50 metres intervals but
% print labels only at 100 metres intervals:
val=[-700:50:600];%Contour lines
val2=[-700:100:600];%Labels

figure(1)
pcolor(xutm,yutm,topobat_50m')
shading flat
hold on
contour(xutm,yutm,topobat_50m',val2,'LineWidth',0.1,'ShowText','on','L
ineColor','k')
set(gca,'Ydir','reverse')
ax = gca;
load('MyColormaps','geog')
colormap(ax,geog)
title('Deception Island topography','FontSize',18);
xlabel('Latitude (UTM)');ylabel('Longitude (UTM)');
colorbar

%Modified topography representation:
figure(2)
pcolor(xutm,yutm,solo_topo');shading flat;
hold on
contour(xutm,yutm,solo_topo',val2,'LineWidth',0.1,'ShowText','on','Lin
eColor','k')
set(gca,'Ydir','reverse')
hold on
contour(xutm,yutm,topobat_50m',[0 0],'LineWidth',0.1,'LineColor','k')
```

```matlab
ax = gca;
load('MyColormaps','geog')
colormap(ax,geog)
title('Corrected Deception Island topography','FontSize',18);
xlabel('Latitude (UTM)');ylabel('Longitude (UTM)');
colorbar

%% Array L %%

%Array representation over the topography:
figure(3)
ax = gca;
load('MyColormaps','geog')
colormap(ax,geog)
pcolor(x,y,topobat_50m');shading flat
hold on
contour(x,y,topobat_50m',val2,'LineWidth',0.1,'Showtext','on','LineCol
or','k')
ax = gca;load('MyColormaps','geog');colormap(ax,geog)
hold on
plot(xstat,ystat,'.k')
title('Synthetic array location','FontSize',18);
colorbar
hold on
plot(x0,y0,'^r')%Posición del centro del array

close all
```

Appendix 2

```matlab
%% TOMOGRAPHIC DATA CORRECTION %%

% Modification of the original data to include the ocean.

% The data file contains three columns (vp, vs, dens), each with
%+16M values. They need to be transformed into a 401x401x101 matrix.

cd('P:\Universidad\TFM\Datos')

%Load data:
datos=load('tomo_original.mat');

load topomats.mat;
topobat=topobat_50m;

%Define variables and create matrices:
vp_dat=datos(:,1);vs_dat=datos(:,2);dens_dat=datos(:,3);

vp_na=reshape(vp_dat,401,401,101);
vs_na=reshape(vs_dat,401,401,101);
dens_na=reshape(dens_dat,401,401,101);

%For those nodes below sea level but above the sea floor surface,
%vp, vs and density need to be corrected. The rest must remain
```

```matlab
untouched.
%There is no need to correct those nodes above sea level and above
%topography, as the finite-difference software ignores them.

%Sea level is placed 4500 metres above the bottom of the domain, which
is
%5050 metres high. On a 50m cell grid, row 11 from the top of the
domain
%defines sea level.

for i=1:401
    for j=1:401

        if topobat(i,j)<0
            %Last row to correct:
            m=abs(topobat(i,j))/50;%Índice de la fila hasta la que hay
que corregir
            %Apply corrections:
            vp_na(i,j,12:m+11)=1500;
            vs_na(i,j,12:m+11)=0;
            dens_na(i,j,12:m+11)=1000;

        end

    end
end


%Transform matrices into columns again and save results:
vp_corr_na=reshape(vp_na,16240901,1);
vs_corr_na=reshape(vs_na,16240901,1);
dens_corr_na=reshape(dens_na,16240901,1);

datos_corr=[vp_corr_na vs_corr_na dens_corr_na];

%Save into a new tomo file:
filename='tomo_20x20x5km_50m_corr_naire.dat';
dlmwrite(filename,datos_corr,'delimiter',' ','newline','unix')

%Save variables:
save('tomo_nocorr_corr_na.mat','x','y','topobat','vp_dat','vs_dat','de
ns_dat','vp_na','vs_na','dens_na','vp_corr_na','vs_corr_na','dens_corr
_na')

%% PLOT SECTIONS TO CHECK CORRECTIONS %%

clear all
load('tomo_nocorr_corr_na.mat')
%vs, vp, dens dat are the original (column) variables
%vs, vp, dens na are the corrected matrices
%vs, vp, dens corr_na are the corrected (column) variables

%Original matrices:
vp_mat=reshape(vp_dat,401,401,101);
vs_mat=reshape(vs_dat,401,401,101);
dens_mat=reshape(dens_dat,401,401,101);

%Top of the domain:
vp_na1=vp_na(:,:,1);
```

```matlab
%200 metres above sea level:
vp_na8=vp_na(:,:,8);vp_mat8=vp_mat(:,:,8);

%Sea level:
vp_na12=vp_na(:,:,12);vp_mat12=vp_mat(:,:,12);

%50 metres deep:
vp_na13=vp_na(:,:,13);vp_mat13=vp_mat(:,:,13);

%100 metres deep:
vp_na14=vp_na(:,:,14);vp_mat14=vp_mat(:,:,14);

%150 metres deep:
vp_na15=vp_na(:,:,15);vp_mat15=vp_mat(:,:,15);

%200 metres deep:
vp_na16=vp_na(:,:,16);vp_mat16=vp_mat(:,:,16);

%700 metres deep:
vp_na26=vp_na(:,:,26);vp_mat26=vp_mat(:,:,26);

%Flip color scale:
colormap(flipud(jet));


%Plot sections:

%UTM distance vectors:
xutm0=610904;ytum0=3007311;%In metres
x2=(0:50:20000);y2=(0:50:20000);
xutm=(xutm0+x2);yutm=(ytum0+y2);

figure(1)
subplot(241)
contour(xutm,yutm,topobat',[0 0],'LineWidth',0.1,'LineColor','k');
hold on;pcolor(xutm,yutm,vp_mat12');shading flat;colorbar;
set(gca,'Ydir','reverse')
title('Vp - original - sea level');
caxis([min(min(vp_mat12)) max(max(vp_mat12))]);

subplot(242)
contour(xutm,yutm,topobat',[0 0],'LineWidth',0.1,'LineColor','k');
hold on;pcolor(xutm,yutm,vp_mat14');shading flat;colorbar;
set(gca,'Ydir','reverse')
title('Vp - original - 100 m below sea level');
caxis([min(min(vp_mat14)) max(max(vp_mat14))]);

subplot(243)
contour(xutm,yutm,topobat',[0 0],'LineWidth',0.1,'LineColor','k');
hold on;pcolor(xutm,yutm,vp_mat16');shading flat;colorbar;
set(gca,'Ydir','reverse')
title('Vp - original - 200 m below sea level');
caxis([min(min(vp_mat16)) max(max(vp_mat16))]);

subplot(244)
contour(xutm,yutm,topobat',[0 0],'LineWidth',0.1,'LineColor','k');
hold on;pcolor(xutm,yutm,vp_mat26');shading flat;colorbar;
set(gca,'Ydir','reverse')
```

```matlab
title('Vp - original - 700 m below sea level');
caxis([min(min(vp_mat26)) max(max(vp_mat26))]);

subplot(245)
contour(xutm,yutm,topobat',[0 0],'LineWidth',0.1,'LineColor','k');
hold on;pcolor(xutm,yutm,vp_na12');shading flat;colorbar;
set(gca,'Ydir','reverse')
title('Vp - corrected - sea level');
caxis([min(min(vp_na12)) max(max(vp_na12))]);

subplot(246)
contour(xutm,yutm,topobat',[0 0],'LineWidth',0.1,'LineColor','k');
hold on;pcolor(xutm,yutm,vp_na14');shading flat;colorbar;
set(gca,'Ydir','reverse')
title('Vp - corrected - 100 m below sea level');
caxis([min(min(vp_na14)) max(max(vp_na14))]);

subplot(247)
contour(xutm,yutm,topobat',[0 0],'LineWidth',0.1,'LineColor','k');
hold on;pcolor(xutm,yutm,vp_na16');shading flat;colorbar;
set(gca,'Ydir','reverse')
title('Vp - corrected - 200 m below sea level');
caxis([min(min(vp_na16)) max(max(vp_na16))]);

subplot(248)
contour(xutm,yutm,topobat',[0 0],'LineWidth',0.1,'LineColor','k');
hold on;pcolor(xutm,yutm,vp_na26');shading flat;colorbar;
set(gca,'Ydir','reverse')
title('Vp - corrected - 700 m below sea level');
caxis([min(min(vp_na26)) max(max(vp_na26))]);
```

Appendix 3

```matlab
%% CREATION OF THE INPUT FILES FOR THE FINITE DIFFERENCE METHOD %%

sims=load('P:\Universidad\TFM\Datos\Simulaciones_1Hz\sims.dat');
zsims=sims(:,3);%Depth of each source

%The first two lines of the files need to be changed for each N-S
series of
%shots. The rest are the same for all sources. Parameter j needs to be
%changed for each series as well (depending on the number of shots).

for j=131:153 %


file=['P:\Universidad\TFM\Datos\Simulaciones_1Hz\source_1Hz_',num2str(
j),'.inp' ];

file2=['P:\Universidad\TFM\Datos\Simulaciones_2Hz\source_2Hz_',num2str
(j),'.inp' ];
```

```matlab
k1=(-1400:300:-500)+10000;    k2=(-1700:300:-200)+10000;
k3=(-1900:300:-100)+10000;    k4=(-1900:300:200)+10000;
k5=(-1900:300:1400)+10000;    k6=(-1900:300:1700)+10000;
k7=(-2200:300:2900)+10000;    k8=(-2200:300:3200)+10000;
k9=(-2500:300:3500)+10000;    k10=(-2800:300:3500)+10000;
k11=(-3100:300:3500)+10000;    k12=(-3400:300:3200)+10000;
k13=(-3700:300:3200)+10000;    k14=(-3700:300:2900)+10000;
k15=(-3700:300:2900)+10000;    k16=(-4000:300:2600)+10000;
k17=(-4300:300:2600)+10000;    k18=(-4300:300:-700)+10000;
k19=(-4300:300:-1000)+10000;    k20=(-4300:300:-3100)+10000;
k21=(-4600:300:-3700)+10000;    k22=(-4600:300:-3700)+10000;


        % Open file - 1Hz:
        fid=fopen(file,'wt');
        %Line 1 - 1Hz: cell dimensions
        fprintf(fid,'%d\n',50);
        %Line 2 - 1Hz: source x coord., source y coord., max.
elevation, source
        %elevation (from sea level)
        fprintf(fid,'%+d %+d %d %+d\n',-1500+10000,k11(j-
130),550,zsims(j));

        % Open file - 2 Hz:
        fid2=fopen(file2,'wt');
        %Line 1: cell dimensions
        fprintf(fid2,'%d\n',50);
        %Line 2: source x coord., source y coord., max. elevation,
source
        %elevation (from sea level)
        fprintf(fid2,'%+d %+d %d %+d\n',-1500+10000,k11(j-
130),550,zsims(j));




        %Line 3: force
        fprintf(fid,'%.1f  %.1f  %.1f\n',0.0,0.0,0.0);
              fprintf(fid2,'%.1f  %.1f  %.1f\n',0.0,0.0,0.0);
        %Line 4: moment tensor
        fprintf(fid,'%.1e  %.1f  %.1f\n',1.0e14,0.0,0.0);
              fprintf(fid2,'%.1e  %.1f  %.1f\n',1.0e14,0.0,0.0);
        %Line 5: moment tensor
        fprintf(fid,'%.1f  %.1e  %.1f\n',0.0,1.0e14,0.0);
              fprintf(fid2,'%.1f  %.1e  %.1f\n',0.0,1.0e14,0.0);
        %Line 6: moment tensor
        fprintf(fid,'%.1f  %.1f  %.1e\n',0.0,0.0,1.0e14);
              fprintf(fid2,'%.1f  %.1f  %.1e\n',0.0,0.0,1.0e14);
        %Line 7: source time function and period
        fprintf(fid,'%d %.1f\n',3,1);
              fprintf(fid2,'%d %.1f\n',3,0.5);
        %Line 8: half-space flag: 1 - data from tomo file / 0- take
vp, vs,
        %density from this line
        fprintf(fid,'%d %d %d %d\n',1,4000,2000,2650);
              fprintf(fid2,'%d %d %d %d\n',1,4000,2000,2650);
        %Line 9: sampling interval and seismogram length in seconds
        fprintf(fid,'%.4f %.0f\n',0.0025,10);
              fprintf(fid2,'%.4f %.0f\n',0.0025,10);
```

```matlab
        %Line 10: decimation factors for snapshots and seismogram
        fprintf(fid,'%d %d %.0f\n',0,25,4);
                fprintf(fid2,'%d %d %.0f\n',0,25,4);
        %Line 11: snapshot flag: 0 - no snapshots / 1 - snapshots and
type of snapshots
        fprintf(fid,'%d %s%s%s\n',0,char(39),'d41',char(39));
                fprintf(fid2,'%d %s%s%s\n',0,char(39),'d41',char(39));
        %Line 12: array coordinates file and number of stations
        fprintf(fid,'%s%s%s
%.0f\n',char(39),'arrayL_mSW.dat',char(39),10);
                fprintf(fid2,'%s%s%s
%.0f\n',char(39),'arrayL_mSW.dat',char(39),10);
        %Line 13: topography file
        fprintf(fid,'%s%s
%s\n',char(39),'topo_2016rounded_20x20km_50m.dat',char(39));
                fprintf(fid2,'%s%s
%s\n',char(39),'topo_2016rounded_20x20km_50m.dat',char(39));
        %Line 14: output file
        fprintf(fid,'%s%s%s%s
%s\n',char(39),'dec','_1Hz_',num2str(j),char(39));
                fprintf(fid2,'%s%s%s%s
%s\n',char(39),'dec','_2Hz_',num2str(j),char(39));
        %Line 15: tomography file
        fprintf(fid,'%s%s
%s\n',char(39),'tomo_20x20x5km_50m_corr_naire.dat',char(39));
                fprintf(fid2,'%s%s
%s\n',char(39),'tomo_20x20x5km_50m_corr_naire.dat',char(39));



end

    fclose(fid);



%% CREATION OF A RUN FILE CALLING THE FIN.DIFF. INPUT FILES %%
%                       1Hz AND 2Hz                          %

file=('P:\Universidad\TFM\Datos\Simulaciones_1Hz\run.csh');

% PRIMERAS LÍNEAS FICHERO 1 HZ:
fid=fopen(file,'wt');

for j=1:331 %number of files

    if j>=1 & j<=9

        fprintf(fid,'%s%d%s\n','./topo_v17 < source_1Hz_00',j,'.inp >
tmp');

    elseif j>=10 & j<=99

        fprintf(fid,'%s%d%s\n','./topo_v17 < source_1Hz_0',j,'.inp >
tmp');

    elseif j>=100
```

```matlab
        fprintf(fid,'%s%d%s\n','./topo_v17 < source_1Hz_',j,'.inp >
tmp');

    end

end

for k=1:331 %number of files

    if k>=1 & k<=9

        fprintf(fid,'%s%d%s\n','./topo_v17 < source_2Hz_00',k,'.inp >
tmp');

    elseif k>=10 & k<=99

        fprintf(fid,'%s%d%s\n','./topo_v17 < source_2Hz_0',k,'.inp >
tmp');

    elseif k>=100

        fprintf(fid,'%s%d%s\n','./topo_v17 < source_2Hz_',k,'.inp >
tmp');

    end

end

fclose(fid);
```

Appendix 4

```matlab
%%                    SEISMOGRAM SEPARATION                        %%

cd('P:\Universidad\TFM\Datos\Simulaciones_1Hz')


%Functions provided by Dr. Javier Almendros:
%     fdseis2sac
%     readsac
%     writesac


%All 10 seismograms are contained within a single file created by the
%finite-difference programme.
%They need to be saved into separate files before analysing them.

files = dir('dec_1Hz_*');
numfiles = length(files)


for K = 1:numfiles
```

```matlab
        fdseis2sac(files(K).name)


end



%%              SAC READING AND MODIFICATION            %%
% I need to add 1000 noise samples before the proper signal begins
% This noise needs to be filtered in order to obtain a more realistic
% signal. The seismogram will thus be 20 seconds long

cd('P:\Universidad\TFM\Datos\Simulaciones_2Hz')

% WARNING!! This code must NOT be executed twice over the same files!
% The modified sac files are saved with the same name the original
ones
% had, they replace the original seismograms.

fnames = dir('*.sac');
numfnames = length(fnames)

%Creation of the filter:
    dt=0.01;%Sampling interval
    fNy=(1/dt)/2;%Nyquist frequency
    [b,a]=butter(2,[0.5 15]/fNy);

    %Create zeros vector:
    ceros=zeros(1000,K);
    %Create noise:
    ruido=2*rand(2001,numfnames)-1;%uniform noise in the [-1 1] range
    %ruido=randn(2001,numfnames);%gaussian noise with mean 0 and std 1
    %Apply filter:
    ruidofilt=filtfilt(b,a,ruido);
    SNR=40;%signal to noise ratio

for K = 1:numfnames

    %Save each sac into a matrix:
    sacmat(:,K)=readsac(fnames(K).name,'pc');
    maxdat=max(abs(sacmat));%maximum amplitude of the seismogram

    %Add zeros:
    sacmat2(:,K)=[ceros(:,K);sacmat(:,K)];

    %Apply filter:
    ruidofilt(:,K)=filtfilt(b,a,ruido(:,K));
    %Add noise to seismograms:
    sacmat3=sacmat2+ruidofilt(:,K)*(maxdat/SNR);%add noise with given
SNR
    %Save sac file:
        % writesac(data,file,platform,delta,tini);
        % data...seismogram
        % file...sac binary file
        % platform...'sun' or 'pc' [default 'pc']
        % delta...sampling interval
        % tini...time of first sample
    writesac(sacmat3(:,K),fnames(K).name,'pc',0.01,0)
```

```
end
```

Appendix 5

```
%% CREATION OF INPUT FILES FOR THE CROSS CORRELATION METHOD %


for j=1:331 %Source number

    % 1Hz:
    %Just change 1Hz for 2Hz to generate those input files.

    if j<10

file1=['P:\Universidad\TFM\Datos\Simulaciones_1Hz\cc_1Hz_00',num2str(j
),'.inp' ];
        fid=fopen(file1,'wt');
        %Line 1: directory containing the seismograms
        fprintf(fid,'%s\n','/home/itahisa/Simulaciones_1Hz/');
        %Line 2: seismogram file name
        fprintf(fid,'%s%s%d%s\n','dec_1Hz_','00',j,'.');
        %Line 3: file extension
        fprintf(fid,'%s\n','.sac');
        %Line 4: number of stations (one + for each station)
        fprintf(fid,'%s\n','++++++++++');
        %Line 5: array coordinates file
        fprintf(fid,'%s\n','/home/itahisa/arrayL_kmSW.dat');
        %Line 6: number of samples to skip at the beginning / number
of
        %samples / frequency range to filter (min, max)
        fprintf(fid,'%d %d %.1f %.d\n',0,2001,0.4,3);
        %Line 7:  apparent slowness interval to consider / app.slow.
grid size
        fprintf(fid,'%.1f %.2f\n',1.5,0.01);
        %Line 8: initial sample number / number of time windows / time
        %windows length / time step (% of time window length)
        fprintf(fid,'%d %d %d %.2f\n',300,139,200,0.05);
        %Line 9: uncertainty threshold
        fprintf(fid,'%.2f\n',0.05);
    elseif j>=10 && j<=99

file1=['P:\Universidad\TFM\Datos\Simulaciones_1Hz\cc_1Hz_0',num2str(j)
,'.inp' ];
        fid=fopen(file1,'wt');
        %Line 1: directory containing the seismograms
        fprintf(fid,'%s\n','/home/itahisa/Simulaciones_1Hz/');
        %Line 2: seismogram file name
        fprintf(fid,'%s%s%d%s\n','dec_1Hz_','0',j,'.');
        %Line 3: file extension
        fprintf(fid,'%s\n','.sac');
```

```matlab
        %Line 4: number of stations (one + for each station)
        fprintf(fid,'%s\n','++++++++++');
        %Line 5: array coordinates file
        fprintf(fid,'%s\n','/home/itahisa/arrayL_kmSW.dat');
        %Line 6: number of samples to skip at the beginning / number
of
        %samples / frequency range to filter (min, max)
        fprintf(fid,'%d %d %.1f %.d\n',0,2001,0.4,3);
        %Line 7:  apparent slowness interval to consider / app.slow.
grid
        %size
        fprintf(fid,'%.1f %.2f\n',1.5,0.01);
        %Line 8: initial sample number / number of time windows / time
        %windows length / time step (% of time window length)
        fprintf(fid,'%d %d %d %.2f\n',300,139,200,0.05);
        %Line 9: uncertainty threshold
        fprintf(fid,'%.2f\n',0.05);
    elseif j>=100

file1=['P:\Universidad\TFM\Datos\Simulaciones_1Hz\cc_1Hz_',num2str(j),
'.inp' ];
        fid=fopen(file1,'wt');
        %Line 1: directory containing the seismograms
        fprintf(fid,'%s\n','/home/itahisa/Simulaciones_1Hz/');
        %Line 2: seismogram file name
        fprintf(fid,'%s%d%s\n','dec_1Hz_',j,'.');
        %Line 3: file extension
        fprintf(fid,'%s\n','.sac');
        %Line 4: number of stations (one + for each station)
        fprintf(fid,'%s\n','++++++++++');
        %Line 5: array coordinates file
        fprintf(fid,'%s\n','/home/itahisa/arrayL_kmSW.dat');
        %Line 6: number of samples to skip at the beginning / number
of
        %samples / frequency range to filter (min, max)
        fprintf(fid,'%d %d %.1f %.d\n',0,2001,0.4,3);
        %Line 7:  apparent slowness interval to consider / app.slow.
grid
        %size
        fprintf(fid,'%.1f %.2f\n',1.5,0.01);
     %Line 8: initial sample number / number of time windows / time
        %windows length / time step (% of time window length)
        fprintf(fid,'%d %d %d %.2f\n',300,139,200,0.05);
        %Line 9: uncertainty threshold
        fprintf(fid,'%.2f\n',0.05);
    end

end

    fclose(fid);




%% CREATION OF A RUN FILE CALLING THE ZLCC INPUT FILES  %
%                      1 AND 2 Hz                       %

file=('P:\Universidad\TFM\Datos\Simulaciones_1Hz\run_cc_1Hz.csh');
file2=('P:\Universidad\TFM\Datos\Simulaciones_2Hz\run_cc_2Hz.csh');
```

```matlab
fid=fopen(file,'wt');
fid2=fopen(file2,'wt');

for j=1:331 %number of files

    if j<10

        fprintf(fid,'%s %s%d%s %s%d
%s\n','/home/itahisa/fk/cc8mre_sac.linux','cc_1Hz_00',j,'.inp','cc_1Hz
_00',j,'.out > tmp');
        fprintf(fid2,'%s %s%d%s %s%d
%s\n','/home/itahisa/fk/cc8mre_sac.linux','cc_2Hz_00',j,'.inp','cc_2Hz
_00',j,'.out > tmp');

    elseif j>=10 && j<=99

        fprintf(fid,'%s %s%d%s %s%d
%s\n','/home/itahisa/fk/cc8mre_sac.linux','cc_1Hz_0',j,'.inp','cc_1Hz_
0',j,'.out > tmp');
        fprintf(fid2,'%s %s%d%s %s%d
%s\n','/home/itahisa/fk/cc8mre_sac.linux','cc_2Hz_0',j,'.inp','cc_2Hz_
0',j,'.out > tmp');

    elseif j>=100

        fprintf(fid,'%s %s%d%s %s%d
%s\n','/home/itahisa/fk/cc8mre_sac.linux','cc_1Hz_',j,'.inp','cc_1Hz_'
,j,'.out > tmp');
        fprintf(fid2,'%s %s%d%s %s%d
%s\n','/home/itahisa/fk/cc8mre_sac.linux','cc_2Hz_',j,'.inp','cc_2Hz_'
,j,'.out > tmp');

    end

end


fclose(fid);fclose(fid2);
```